Journal of Hydrology: Regional Studies 66 (2026) 103534

Contents lists available at ScienceDirect

Journal of Hydrology: Regional Studies

journal homepage: www.elsevier.com/locate/ejrh

Multi-timescale streamflow projections in human-regulated basins of southwest Iran using CWatM and explainable machine learning

Mahdi Mohammadnezhad [a,1], Ali Rezaee [a,2], Mikhail Smilovic [b,c,*,3]

[a] Water Science and Engineering Department, College of Agriculture, Ferdowsi University of Mashhad, P. O. Box: 9177948974, Mashhad, Iran
[b] Water Security Research Group, Biodiversity and Natural Resources Program, International Institute of Applied Systems Analysis (IIASA), Schlossplatz 1, Laxenburg A-2361, Austria
[c] Chair of Hydrology and Water Resources, ETH Zurich, Zurich 8049, Switzerland

ARTICLE INFO

Keywords:
Streamflow
CWatM
SSP Scenarios
Uncertainty
Climate change
GloFAS
Hydrological extremes

ABSTRACT

Study region: The Karun-Karkheh-Marzi-e-Gharb river basin complex, a strategically vital but data-scarce and human-regulated region in Western Iran characterized by semi-arid conditions and complex topography.
Study focus: This research evaluates future hydroclimatic shifts by integrating the Community Water Model (CWatM) with a dual-benchmark calibration framework. The study utilizes a computationally efficient strategy—reducing runtime by 55%—to enable a 30-member ensemble projection (General Circulation Models) without high-performance computing. To address anthropogenic non-stationarity and data constraints, the model was validated against both a naturalized benchmark (KGE=0.71) and regulated local observations (KGE=0.60). Furthermore, SHAP-based sensitivity analysis, validated by high-accuracy surrogate models, including XGBoost (R2=0.98, RMSE=0.04) and Linear Regression (R2 =0.95, RMSE=0.1), was employed to quantify the influence of physical and anthropogenic drivers on the basin's hydrological response.
New hydrological insights for the region: Projections reveal a consistent hydrograph transformation driven by thermal forcing across all scenarios. Warmer winters are projected to reduce snow storage, advancing peak flow timing toward late winter. Crucially, intensified evapotranspiration is found to outweigh precipitation variability, shifting the basin from a storage-controlled to an evaporation-dominated system. This leads to declining annual water yields and escalating late-century drought extremes. These findings provide a refined, physically-based projection that potentially extends beyond traditional national climatic reports, suggesting that regional water security should prioritize demand-side management and a transition from stationary allocation rules toward adaptive, climate-resilient strategies.

* Corresponding author at: Chair of Hydrology and Water Resources, ETH Zurich, Zurich 8049, Switzerland.
E-mail addresses: mohammadnezhad@alumni.um.ac.ir (M. Mohammadnezhad), ali_rezaee72@alumni.um.ac.ir (A. Rezaee), smilovic@iiasa.ac.at (M. Smilovic).
[1] ORCID Num: 0009-0001-1878-7185
[2] ORCID Num: 0000-0002-2018-1043
[3] ORCID Num: 0000-0001-9651-8821

https://doi.org/10.1016/j.ejrh.2026.103534
Received 8 April 2026; Received in revised form 28 April 2026; Accepted 8 May 2026
Available online 20 May 2026

1. Introduction

Effective water resource management is paramount for global sustainability as growing populations and escalating droughts place increasing pressure on all water balance components (Zhu et al., 2025). In this context, artificial intelligence (AI) and advanced modeling frameworks have proven to be powerful tools for modeling complex, non-linear hydrological processes (Chang et al., 2023; Granata, 2019). Recent advancements emphasize the integration of process-driven and data-driven models into hybrid systems to capture both physical and non-linear relationships more effectively (Zhu et al., 2025; Ayele and Yu, 2025). However, in anthropogenically stressed environments, hydrological uncertainty is primarily driven by the inherent inaccuracies and lack of precision in observational records, which are often severely compromised by unquantified upstream regulations and non-naturalized water balances (Samaniego et al., 2017; Du et al., 2016). In such regulated contexts, these data limitations typically overshadow the uncertainties arising from model structure and parameterization schemes (Samaniego et al., 2017; Beven, 2001).

The management of water resources is increasingly challenged by the combined impacts of climate change and anthropogenic regulations (Huntington, 2006; Dione et al., 2024). Human activities—including reservoir operations and groundwater abstraction—have fundamentally modified the natural cycle, creating "non-naturalized" water balances (Du et al., 2016). In such human-regulated catchments, traditional modeling often fails to account for river-scale attributes like the degree of regulation and dam density, which are critical for accurate streamflow prediction (Tursun et al., 2024). Recent studies highlight that while machine learning models can help reconstruct naturalized flow in arid basins, their performance is heavily dependent on data quality and the ability to distinguish climate signals from human-induced alterations (Wang et al., 2025; Khan et al., 2023).

To address these complexities, modular modeling approaches like the Framework for Understanding Structural Errors (FUSE) and the Catchment Modelling Framework (CMF) offer flexibility in testing hydrologic hypotheses (Clark et al., 2015). However, while FUSE primarily diagnoses structural differences in natural systems (Clark et al., 2008) and CMF focuses on assembly-based model construction (Kraft et al., 2011), the Community Water Model (CWatM) was selected for this research. CWatM is uniquely suited for human-impacted environments, explicitly incorporating reservoir regulations and irrigation withdrawals directly into the rainfall-runoff process (Burek et al., 2019). Recent comparisons have shown that CWatM provides discharge estimations that align more closely with observations than many other global models, making it the most robust choice for modeling highly regulated basins (Burek et al., 2019).

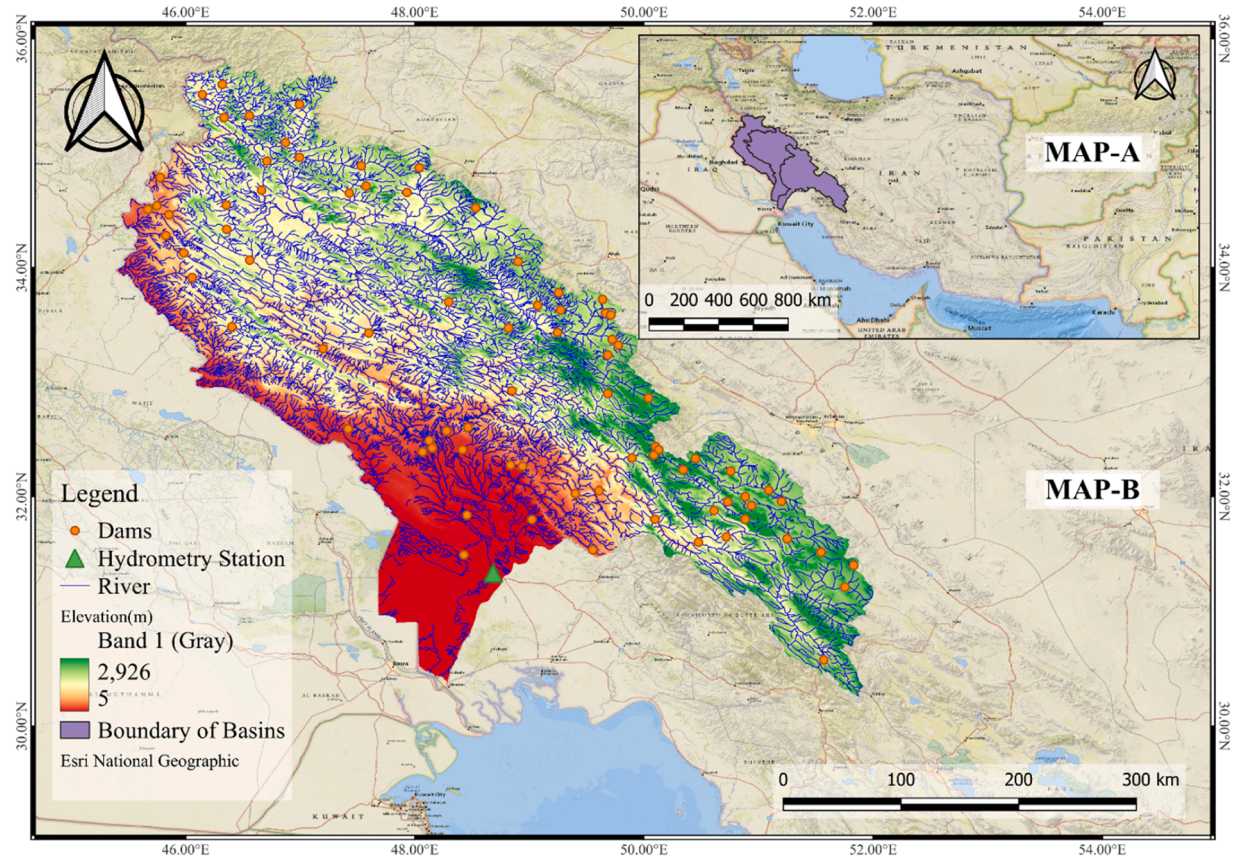

Fig. 1. Location of the case study in Iran. (A) The country of Iran; (B) Digital Elevation Model and stream network of the study area, showing the hydrometry station and dams.

The integrated Great Karun, Karkheh, and Marzi-e-Gharb basin complex was selected for this study due to its strategic importance for Iran's food and energy security and its status as a highly anthropogenically stressed system (Abdi-Dehkordi et al., 2024). To provide robust and actionable insights for this strategically vital region, this research introduces a multi-faceted modeling framework that addresses key gaps in regulated basin hydrology. As a pioneering effort for the Ministry of Energy and regional authorities, these insights provide the necessary documented background to navigate hydroclimatic volatility and guide strategic policy-making in the distant future. A core novelty of this study is the implementation of a dual-benchmark calibration strategy, which evaluates model performance against both local regulated observations (M_{obs}) and global naturalized GloFAS data (M_{bench}). This approach significantly enhances the reliability of climate impact assessments by accounting for the inherent uncertainties in human-altered flow records and observational data. To manage the immense computational demands of processing large-scale ensemble data, a high-performance execution framework was developed using a Rust-based environment, which significantly increased simulation speed and ensured superior computational performance on mid-range systems.

In addressing hydrological uncertainty, a multi-model ensemble of five General Circulation Models (GCMs) across various SSP scenarios is utilized to capture the range of future climatic forcing. By quantifying and presenting the minimum, maximum, and ensemble mean across daily, monthly, seasonal, and annual scales, the full spectrum of predictive uncertainty and the magnitude of extreme events are preserved. To enhance the transparency of this process, Explainable AI (XAI) via the SHAP method is briefly integrated to identify the directional impact of calibrated parameters on model performance (Madhushani et al., 2024; Zhu et al., 2025; Zounemat-Kermani and Kheimi, 2026).

The ultimate objective of this study is to provide a validated, scalable framework for long-term water allocation and the identification of extreme event trends (floods and droughts). By delivering high-accuracy projections of shifts in runoff timing and the intensification of hydroclimatic extremes, this research provides a scientific foundation for dynamic irrigation scheduling and strategic policy-making. These insights are designed to guide the Ministry of Energy and regional authorities in navigating the escalating volatility of the Karun-Karkheh-Marzi-e-Gharb basin complex throughout the 21st century.

2. Methodology

2.1. Case Study

The integrated Great Karun, Karkheh, and Marzi-e-Gharb basin complex (152,971 km^2) was selected as the primary focus for streamflow projection due to its status as the most strategically vital hydrological system in Iran (Ghobadi et al., 2015). This region (Fig. 1) is the nation's principal hub for water, food, and energy security, supporting approximately 9% of the country's total irrigated land (0.6 Mha) and housing the majority of its hydropower capacity (Ghobadi et al., 2015). The basin is characterized by an exceptionally high density of anthropogenic regulations, including massive multi-objective dam networks and intricate irrigation systems,

Table 1
Characteristics and Integration of Global Datasets Used in the CWatM.

Dataset	Source	Original spatial resolution
Elevation	SRTM (Jarvis et al., 2008); Hydro 1k (Geological Survey Center for Earth Resources Observation and Science USGS, 2002)	3″, 1 km
Flow direction map	DDM30 (Döll and Lehner, 2002); DRT (Wu et al., 2011)	30′
Lakes and reservoirs	HydroLakes database (Messager et al., 2016; Lehner et al., 2011)	Shapefile
Soil	Harmonized World Soil Database 1.2 (HWSD) (Fao, ISRIC et al., 2012)	30″
Soil pedotransfer	Rosetta3 (Zhang and Schaap, 2017)	-
Groundwater	GLHYMPS (Gleeson et al., 2011, 2014) (Huscroft et al., 2018)	
Land cover	Forest land cover (Hansen et al., 2013)	1″
	Impervious area (Elvidge et al., 2007)	30″
	Irrigated areas (Döll and Siebert, 2002) (Siebert et al., 2005,2010)	5′
	Hyde 3.2 database (Klein Goldewijk et al., 2017)	5′
Crop coefficient	MIRCA2000 (Portmann et al., 2010)	5′
Albedo	GlobAlbedo dataset (Muller et al., 2012)	3′
Discharge	GRDC (GRDC, 2007)	Station
Population and GDP	Hyde 3.2 database (Klein Goldewijk et al., 2017)	And 5′
	SSP Database at IIASA (Riahi et al., 2017)	County
	SSP population and GDP projections:	7.5′, 30″
	Spatial disaggregation on 30 and 50 (Jones and O'Neill, 2016; Gao, 2017; Kummu et al., 2018; and Gidden et al., 2018)	
Livestock water demand	Gridded livestock densities (Wint and Robinson, 2007; Steinfeld et al., 2006)	5′
	Livestock per country (Fao, ISRIC et al., 2012)	
Industry water demand	Gridded industrial water data (Siklomanov, 1997)	5′
Domestic water demand	domestic water withdrawal per capita (Fao, ISRIC et al., 2012; Gleick and Cooley, 2009)	5′
Global Flood Awareness System (GloFAS) historical dataset	GloFAS (Grimaldi et al., 2022)	0.05′
Meteorological forcing	GSWP3 (Kim et al., 2012)	30′

which have fundamentally altered its natural flow regime (Marjanizadeh et al., 2010; Masih et al., 2011). Given its extreme hydro-climatic gradients—with elevations ranging from 5 to over 2900 m—accurate future discharge projections are essential for this region to balance flood risk management with increasing irrigation demands (Ahmad et al., 2009). The selection of this basin complex is justified by its status as the most anthropogenically stressed and economically significant watershed in the country, providing a critical environment for evaluating future water availability under extreme climatic and human-induced pressures.

2.2. Data acquisition and climate forcing

The CWatM framework integrates diverse global gridded datasets covering topography, land cover, soil properties, and socio-economic parameters to drive geographically detailed simulations (Table 1). Meteorological forcing is the primary driver for rainfall-runoff processes and evapotranspiration estimation. To ensure consistency, all ancillary inputs were systematically harmonized to match the spatial resolution of the primary climate variables.

2.2.1. Historical data and observational data

Historical climate forcing (1981–2019) was derived from the ISIMIP3b dataset at a $0.5^\circ \times 0.5^\circ$ resolution. A statistical summary of this bias-corrected climate dataset (Cucchi et al., 2020) is provided in Table 2. For model calibration and validation, daily discharge records for the Ahvaz gauging station (2006–2016) were obtained from the Global Runoff Data Centre (GRDC) (GRDC, 2007). This station (Latitude: 31.33, Longitude: 48.68) serves as a critical observation point for the basin's outflow (Fig. 1).

2.2.2. Future projections and ensemble strategy

To quantify future hydrological shifts up to 2100, the model was forced with a multi-model ensemble of five GCMs from the ISIMIP3b (CMIP6) collection from 2015 to 2100, specifically GFDL-ESM4, IPSL-CM6A-LR, MPI-ESM1–2-HR, MRI-ESM2–0, and UKESM1–0-LL. The full details, including the model resolution and foundational references, are presented in Table 3. These models were selected for their structural independence and representative range of climate sensitivities, covering both low and high sensitivity to radiative forcing (Lange, 2019; 2021). The climate forcing encompasses three Shared Socioeconomic Pathways (SSPs) representing distinct global development trajectories: the sustainable, low-emission SSP1–2.6; the fragmented, high-challenge SSP3–7.0; and the high-emission SSP5–8.5 (Dione et al., 2024). This multi-model, multi-scenario approach ensures that the simulations capture the full spectrum of GCM and SSP variability inherent in future climate forcing. By utilizing the ISIMIP3b projections directly, the framework accounts for climate uncertainties while maintaining the internal consistency of the bias-corrected GCM outputs.

2.3. CWatM Model Architecture and Modules

The Community Water Model (CWatM) is a comprehensive, modular, and grid-based hydrological framework that incorporates the fundamental processes of surface and groundwater hydrology (Burek et al., 2019). Developed by the International Institute for Applied Systems Analysis (IIASA), the model measures water availability, anthropogenic water use, and the impact of water infrastructure—including reservoirs, groundwater pumping, and irrigation (Burek et al., 2019). CWatM integrates established concepts from the PCR-GLOBWB and LISFLOOD models, enabling an explicit representation of the complete hydrological cycle from snowmelt to groundwater storage (Burek et al., 2019).

For this study, the model was configured at a 0.5° spatial resolution with a daily temporal resolution, utilizing sub-daily time stepping for soil water dynamics and river routing to accurately capture flow behavior (Burek et al., 2019). While this resolution is coarse for detailed reservoir operational modeling—which also requires sensitive sub-daily operational data that is currently unavailable—it is highly suitable for the primary objectives of this study. This spatial scale is sufficient for basin-wide water allocation planning, identifying long-term trends in future extreme events, and large-scale irrigation scheduling, providing a suitable scientific basis for strategic regional policy-making. Fig. 2 provides a schematic representation of the processes in the CWatM model.

Table 2
Statistical description of the climate variables for the historical period (1981–2019).

Parameter (Unit)	Abbreviation	Mean	std	Min	Max	Median
Near-Surface Relative Humidity(%)	hurs	45.55	23.55	5.77	99.12	42.87
Near-Surface Specific Humidity($kgkg^{-1}$)	huss	0.005	0.002	0.0004	0.015	0.005
Precipitation($mmday^{-1}$)	pr	1.43	5.15	0	111	0
Snowfall Flux($mmday^{-1}$)	prsn	0.189	1.39	0	46	0
Surface Air Pressure(Pa)	ps	89991.57	5959.24	80141.51	101444.64	90560.88
Surface Downwelling Longwave Radiation(Wm^{-2})	rlds	302.91	44.86	151.94	433.39	303.13
Surface Downwelling Shortwave Radiation(Wm^{-2})	rsds	230.30	84.30	10.30	364.20	240.00
Near-Surface Wind Speed(ms^{-1})	sfc Wind	2.40	0.99	0.53	11.17	2.20
Near-Surface Air Temperature(K)	tas	290.18	10.90	251.74	314.92	290.20
Daily Maximum Near-Surface Air Temperature(K)	tasmax	297.63	12.19	257.53	324.64	297.81
Daily Minimum Near-Surface Air Temperature(K)	tasmin	282.26	9.44	244.56	306.69	282.36

Table 3
Characteristics of General Circulation Models (GCMs) Used in the ISIMIP3b Ensemble.

GCM	Resolution	Institute	Nation	Reference
GFDL-ESM4	1.0°	NOAA Geophysical Fluid Dynamics Laboratory	USA	(Dunne et al., 2020)
IPSL-CM6A-LR	2.0°	Institut Pierre Simon Laplace	France	(Boucher et al., 2020)
MPI-ESM1–2-HR	1.0°	Max-Planck Institute for Meteorology	Germany	(Mauritsen et al., 2019)
MRI-ESM2–0	1.0°	Meteorological Research Institute	Japan	(Yukimoto et al., 2019)
UKESM1–0-LL	2.0°	Met Office Hadley Centre	UK	(Sellar et al., 2019)

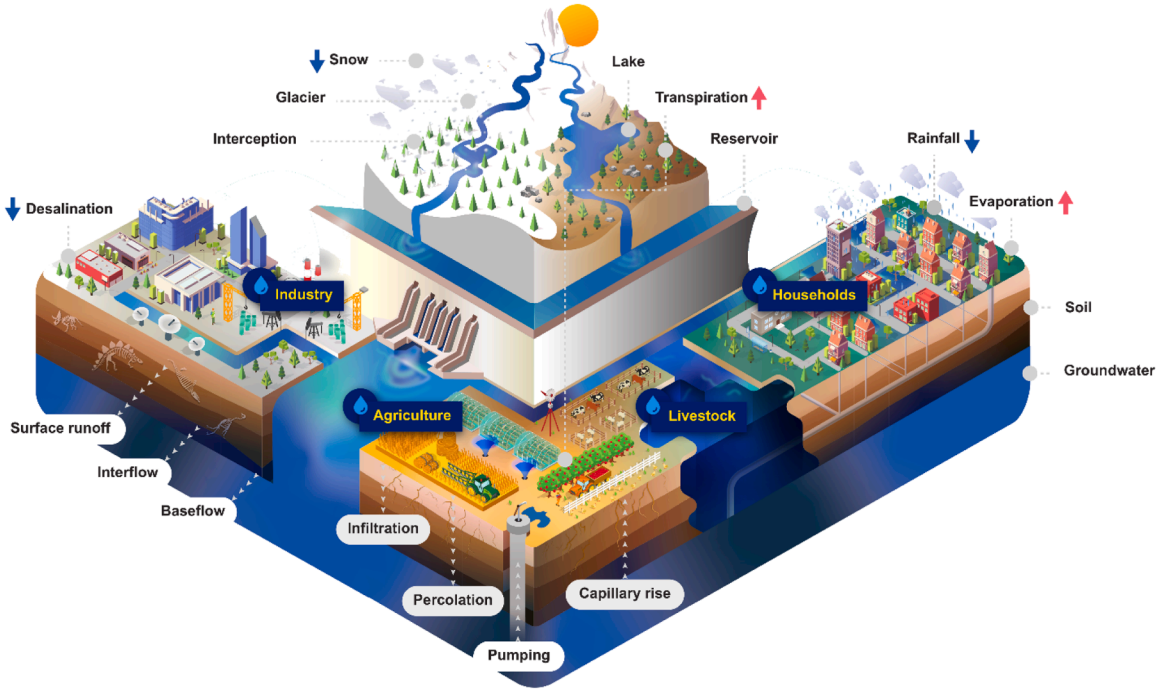

Fig. 2. Schematic illustrating the integrated hydrological and water use processes within the CWatM framework (Burek et al., 2019).

2.4. Computational optimization and execution strategy

To ensure numerical stability and computational efficiency in processing the multi-model ensemble, a robust execution pipeline was developed. This framework utilized the high-performance uv package manager to minimize execution overhead and optimize dependency resolution during the large-scale simulation phases. This optimization enabled the scalable execution of 2250 simulation years (5 GCMs across 3 SSPs) on standard infrastructure. For a detailed description of the computational environment and automation routines, please refer to the Supplementary Material.

2.5. Calibration and multi-criteria benchmarking strategy

The calibration of CWatM is essential to surmount uncertainties inherent in input datasets, parameterization schemes, and grid cell heterogeneity (Samaniego et al., 2017). This process is particularly crucial for basins under intense anthropogenic influence, where realistic simulations are required to support water security and infrastructure management. A significant challenge in such environments stems from the high uncertainty of observational records, as available discharge data are often subject to errors caused by numerous upstream dams and undocumented anthropogenic flow regulations. To address these limitations, a high-performance calibration pipeline was implemented using the NSGA-II evolutionary algorithm (Deb et al., 2002) within the DEAP framework (Fortin et al., 2012), leveraging parallel processing to ensure computational efficiency.

The Modified Kling-Gupta Efficiency (KGE') (Kling et al., 2012) was utilized as the single-objective function for the calibration. As shown in Eq. (1), KGE' provides a comprehensive performance assessment by calculating the Euclidean distance from the ideal point based on three integrated components (Kling et al., 2012; Gupta et al., 2009; Hrachowitz et al., 2013): the correlation coefficient (r), bias ratio (β), and variability ratio (γ):

$$KGE' = 1 - \sqrt{(r-1)^2 + (\beta-1)^2 + (\gamma-1)^2} \quad (1)$$

In this formulation, the bias ratio (β) is defined as the ratio of the mean simulated runoff (μ_s) to the mean observed runoff (μ_0), as expressed in Eq. (2):

$$\beta = \frac{\mu_s}{\mu_0} \tag{2}$$

The variability ratio (γ), according to Eq. (3), is calculated as the ratio of the coefficient of variation of the simulated runoff (CV_s) to that of the observed runoff (CV_0), which is further derived from their respective standard deviations (σ) and means (μ):

$$\gamma = \frac{CV_s}{CV_0} = \frac{\sigma_s/\mu_s}{\sigma_0/\mu_0} \tag{3}$$

The calibration involved three consecutive stages with expanding population and pool sizes to ensure objective function convergence, totaling 5955 simulations. Specifically, the final optimization stage employed a general population size (μ) of 256, a pool size of 6, and 128 runs per generation (λ) over 40 generations, which proved sufficient to yield stable parameter sets. All simulations were executed at a 30-arc-minute spatial resolution over a 20-year period (10 years of spin-up and 10 years for evaluation). These intensive computational tasks were performed on a 12-core machine, with each complete 20-year simulation taking approximately one hour to execute.

To further account for the limitations of local records in anthropogenically stressed basins, a two-stage best model selection was employed. This dual-criteria approach resulted in the identification of two distinct optimal parameter sets: the Observational Best Model (M_{obs}), selected based on the highest KGE' against local GRDC discharge observations, and the Benchmark Best Model (M_{bench}), identified by comparing all calibrated parameter sets against the Global Flood Awareness System (GloFAS) historical time series (produced by forcing the open-source LISFLOOD hydrological model with ERA5 reanalysis data). GloFAS serves as a validated global benchmark that compensates for potential localized observational errors (Hirpa et al., 2018). This dual selection process yielded two optimal parameter sets that were carried forward to the future projection phase, effectively accounting for the inherent limitations of local observational records.

2.6. Future projection and ensemble analysis framework

To assess future hydrological shifts, the two optimal parameter sets—M_{obs} and M_{bench}—were integrated with climate projections from five GCMs across three SSP scenarios, generating an ensemble of 30 unique transient simulations (2015–2100). To quantify the projection spread while minimizing the influence of individual model outliers, a collective ensemble-based approach was used. The Ensemble Mean for each period was calculated by averaging the annual means across the five GCMs. Similarly, the Ensemble Maximum and Minimum (representing the uncertainty envelope) were derived by averaging the respective annual extremes from each of the five ensemble members. This methodology ensures that the reported range reflects the collective internal variability and hydroclimatic volatility projected by the entire multi-model ensemble.

2.7. Global sensitivity analysis using machine learning interpretability

To evaluate the influence of the nine optimized parameters on the model's performance (KGE'), a formal global sensitivity analysis was conducted using a machine learning-based interpretability framework. This analysis utilized SHAP (SHapley Additive exPlanations) values to quantify the contribution of each parameter to the hydrological output. To comprehensively explore the parameter space, two distinct surrogate models were trained to emulate the relationship between the calibrated parameters and the final KGE' values: a high-performance XGBoost model and a Linear Regression model. This dual-modeling approach was selected to differentiate between the purely linear contributions of each parameter and the complex, non-linear interaction effects captured by the tree-based ensemble architecture of XGBoost.

The SHAP values were calculated across the entire ensemble of 5955 calibration runs, providing a robust measure of both the relative importance and the directional impact (positive or negative) of each parameter on model accuracy. By comparing the results from both the linear and non-linear surrogate models, the analysis determines whether the dominant sensitivities in anthropogenically-impacted basins are primarily linear or driven by non-linear interaction effects between soil, groundwater, and land-use parameters. This framework not only validates the calibration process but also provides a deeper understanding of the internal dynamics of CWatM within highly regulated hydrological systems.

2.8. Results evaluation and performance metrics

To ensure a comprehensive assessment of the CWatM's performance beyond the primary objective function (KGE') used during calibration, a suite of widely accepted statistical metrics was utilized to evaluate the simulated discharge against observed and benchmark data. These metrics provided a multifaceted view of model accuracy, bias, and correlation.

The key performance metrics used in this study are given in Eqs. (4)-(6), respectively.

$$R^2 = \left[\frac{\sum_{i=1}^{n}(P_i - P)(O_i - \overline{O})}{\sqrt{(\sum_{i=1}^{n}(P_i - P)^2 (\sum_{i=1}^{n}(O_i - \overline{O})^2)}} \right]^2 \tag{4}$$

$$NSE = 1 - \frac{\sum_{i=1}^{n}(O_i - P_i)^2}{\sum_{i=1}^{n}(O_i - \overline{O})^2} \tag{5}$$

$$RMSE = \sqrt{\frac{\sum_{i=1}^{n}(O_i - P_i)^2}{n}} \tag{6}$$

$$MAE = \frac{\sum_{i=1}^{n}|O_i - P_i|}{n} \tag{7}$$

$$Bias = \frac{\sum_{i=1}^{n}(O_i - P_i)}{\sum_{i=1}^{n}(O_i)} \tag{8}$$

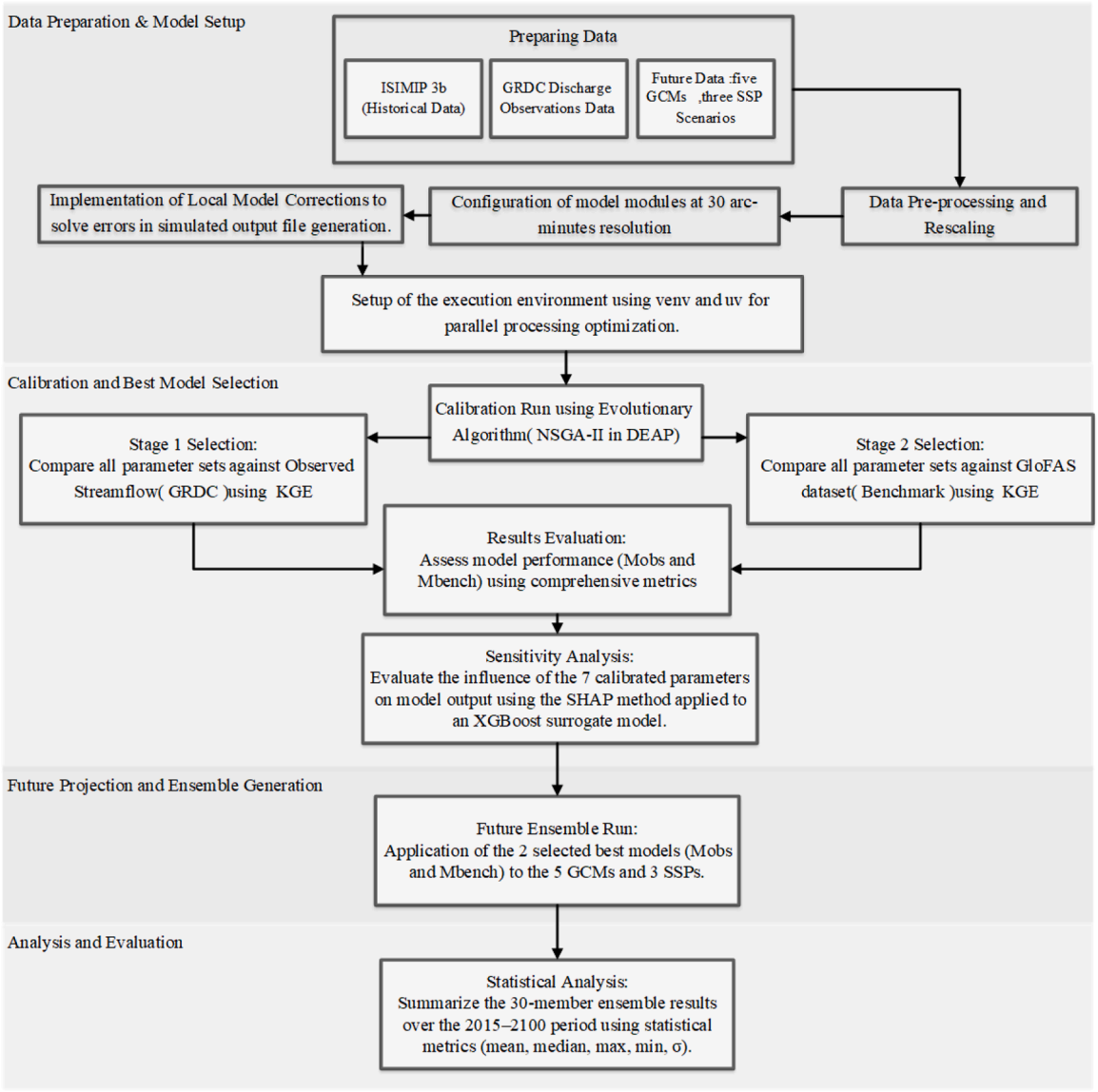

Fig. 3. Overall workflow of the proposed methodology.

$$NS\log = 1 - \frac{\sum_{i=1}^{n}(\ln(O_i) - \ln(P_i))^2}{\sum_{i=1}^{n}(\ln(O_i) - \ln(\overline{O}))^2} \quad (9)$$

Where n is the number of observations, P_i and O_i are the simulated and observed flows at time i, and $\overline{P}$ and $\overline{O}$ are the mean simulated and mean observed flows, respectively.

2.9. Methodological workflow overview

To synthesize the multi-stage integration of data processing, model customization, and ensemble evaluation, a comprehensive workflow is illustrated in Fig. 3. The methodology follows a sequential framework divided into four primary phases: (i) Data Acquisition and Pre-processing, (ii) Two-Stage Calibration and Model Selection, (iii) Ensemble Future Projections, and (iv) Multi-Criteria Performance Evaluation and Sensitivity Analysis. This structured roadmap demonstrates the systematic adaptation of the CWatM to quantify hydrological shifts in anthropogenically-impacted basins and ensures the reproducibility of the computational and analytical steps.

3. Results

3.1. Technical validation and calibration convergence

The implementation phase began with the completion of data acquisition and pre-processing, which included the necessary spatial harmonization and rescaling of all meteorological variables to ensure consistency across the 30-arc-minute grid. Following this, the initial CWatM structure was configured for anthropogenically-impacted basins, requiring specific structural adjustments to maintain validity under regulated flow regimes. Preliminary simulations on mid-range hardware (Intel Core i7–8700K, 64 GB RAM) identified intermittent I/O (Input/Output) inconsistencies during large-scale execution, which were successfully resolved by implementing an automated corrective pipeline that stabilized the model's performance across the entire calibration campaign.

The three-stage evolutionary calibration framework explored the vast parameter space through 5955 simulations, achieving robust convergence as documented in Table 4. The convergence trajectory, illustrated in Fig. 4, shows a sharp initial increase in KGE' scores before stabilizing at a maximum of approximately 0.60. This stabilization confirms that the NSGA-II algorithm effectively reached the Pareto front, identifying stable parameter solutions despite the complexities of human-induced flow alterations and unquantified regulation events.

The adoption of a dual-model selection strategy (M_{obs} and M_{bench}) is justified by both the exhaustive nature of the initial calibration and the significant uncertainty in local observational records. Since the 5955 simulations meticulously explored virtually all possible parameter states, the M_{bench} set could be identified from the existing converged pool without requiring a separate recalibration against GloFAS data. This approach is essential because local discharge records are severely compromised by anthropogenic interventions, such as unquantified upstream dam releases, which prevent station data from accurately representing naturalized flow. By utilizing the globally-validated GloFAS-LISFLOOD time series as a secondary benchmark, the framework effectively mitigates measurement and regulation errors, ensuring a more robust model selection for long-term projections.

The final optimization yielded two distinct sets for the nine key parameters (Table 5), governing processes such as evapotranspiration (Crop Coefficient), soil dynamics (Soil Depth Factor), and groundwater interaction (Recession Coefficient). The systematic optimization of these factors, particularly those related to interflow and runoff concentration, ensures the model captures the temporal delays and discharge reductions typical of highly regulated basins, providing a scientifically suitable foundation for the subsequent ensemble climate projections. Regarding reservoir representation, the lakeAFactor was maintained at its default value of 1.0 to utilize CWatM's standard physical formulations and weir coefficients. Rather than implying a lack of reservoir impact, this approach relies on the model's integrated reservoir operation schemes—governed by storage limits and hydro-physical constraints—to simulate the buffering effects of regulated water bodies without introducing the risks of over-parameterization in the absence of local daily operational data.

3.2. The statistical performance and hydrograph analysis

The evaluation of the two optimal parameter sets, M_{obs} and M_{bench}, demonstrates their respective capacities to replicate distinct aspects of the basin's hydrological regime. Time series analysis (Fig. 5 and Fig. 6) reveals that M_{obs} effectively captures the timing and magnitude of daily discharge during low-to-moderate flow periods. However, it tends to underestimate high-frequency variability and

Table 4
Configuration of the Evolutionary Algorithm for the Multi-Stage Model Calibration.

Run	Population Size (μ)	Pool Size	runs per generation (λ)	Generations
Run 1 (Initial)	16	4	8	6
Run 2 (Expansion)	128	6	32	12
Run 3 (Final)	256	8	128	40

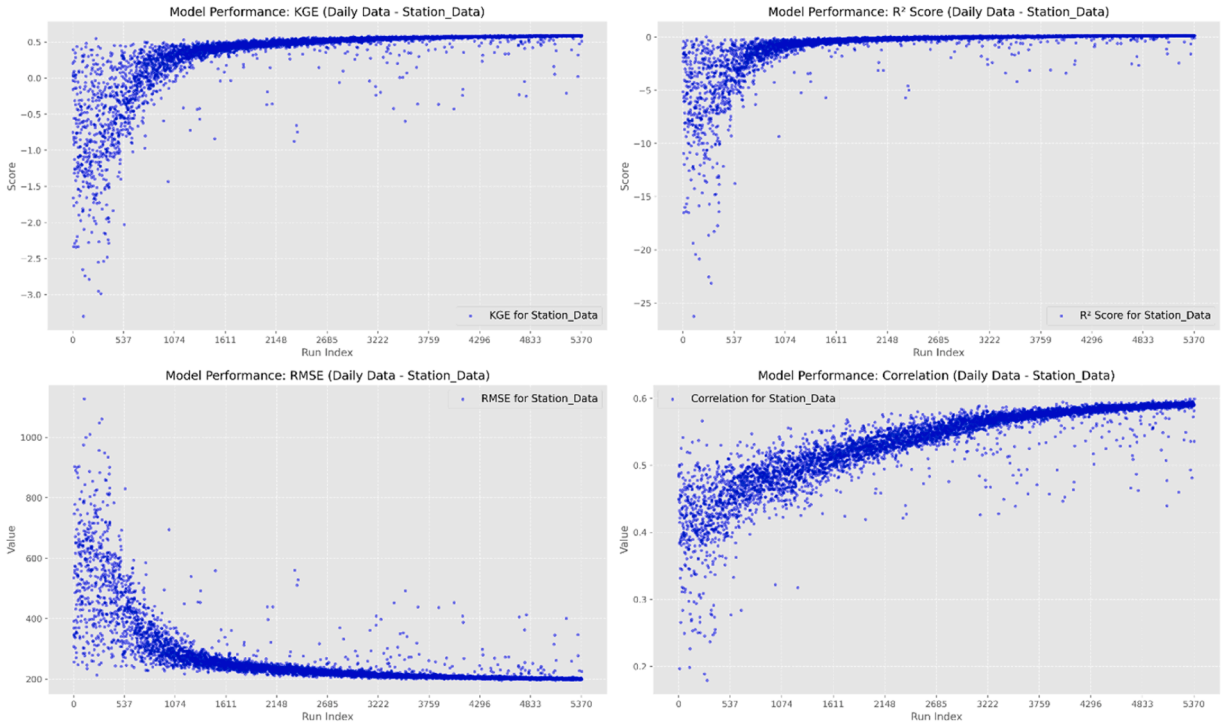

Fig. 4. Model Convergence and Performance Metrics.

Table 5
Final Optimized Values for the Nine Calibrated Parameters in M_{obs} (Observed Data) and M_{bench}(GloFAS Benchmark Data). All listed parameters are dimensionless coefficients.

Parameter	Abbreviation	M_{obs}	M_{bench}
Crop Coefficient	crop_correct	1.76	0.83
Soil Depth Factor	soildepth_factor	1.5	1.33
Preferential Bypass Flow	preferentialFlowConstant	3.08	2.12
Infiltration capacity parameter	arnoBeta_add	0.01	0.80
Interflow Factor	factor_interflow	0.33	2.41
Recession Coefficient Factor	recessionCoeff_factor	3.97	5.84
Runoff Concentration Factor	manningsN	10.0	0.84
Normal storage limit	normalStorageLimit	0.85	0.75
Lake factor	lakeAFactor	1	1

peak flood events, a common inherent consequence of calibrating against highly regulated, non-naturalized flow data. In contrast, the M_{bench} model exhibits superior fidelity in reproducing high-magnitude flows and total discharge volumes. This confirms that M_{bench} provides a robust representation of the naturalized flow regime, which is less compromised by local measurement errors and anthropogenic regulations than the station-based observations.

The multi-faceted statistical evaluation (Table 6) highlights the trade-offs between local optimization and benchmark-driven fidelity. The M_{obs} model achieved a KGE' of 0.60 and a correlation of 0.60, yet showed limitations in capturing residual variance, as indicated by a low NSE of 0.151. Conversely, the M_{bench} model demonstrated markedly superior performance across nearly all metrics, with a KGE', R^2, and NSE all reaching 0.71. Although M_{bench} exhibits higher absolute error metrics (RMSE: 683.3 m^3/s) compared to M_{obs} (RMSE: 199 m^3/s), this discrepancy primarily reflects the difference in flow scales between the large-scale GloFAS benchmark and the regulated local records. These results confirm that M_{obs} is heavily influenced by localized observational limitations, thereby justifying the strategic inclusion of M_{bench} to ensure a more robust and comprehensive range of future climate change projections.

While a significantly superior statistical performance is demonstrated by M_{bench} (KGE = 0.71), which is considered a more robust scientific criterion for identifying hydrological trends, M_{obs} is intentionally retained in this study. The use of M_{bench} was necessitated by the inherent structural uncertainties and potential measurement errors identified within the local observational data. However, M_{obs} is preserved as a necessary benchmark to acknowledge the inherent observational uncertainties and significant data constraints present in the local monitoring network. Therefore, both models are presented to establish a realistic uncertainty envelope that bridges the gap between naturalized potential and anthropogenically-modified flow, ensuring that the projections are grounded in the basin's actual data constraints. Ultimately, M_{bench} is prioritized as the primary reference for interpreting long-term climate impacts due to its higher

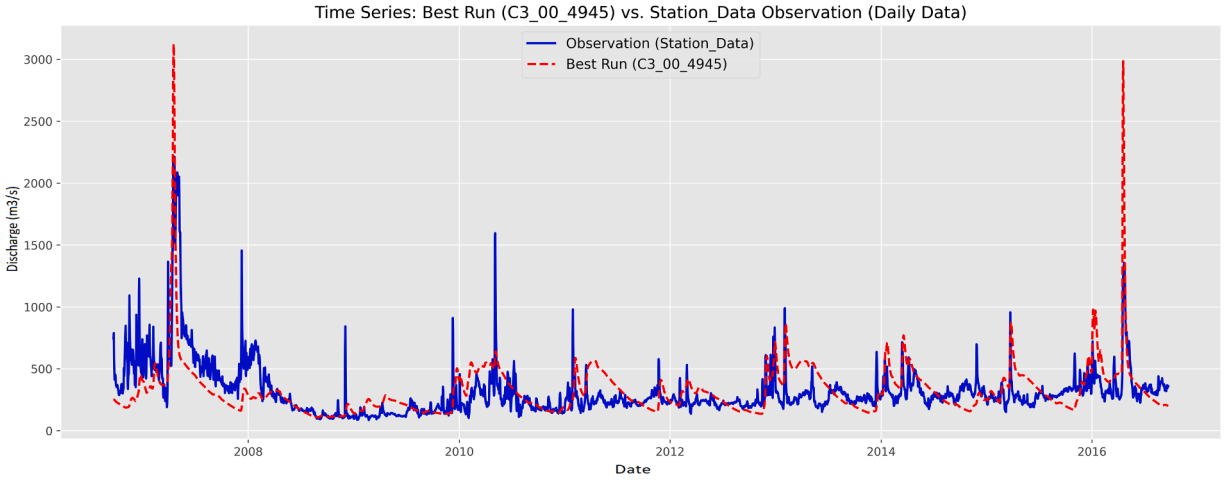

Fig. 5. Simulated vs. Observed Time Series for the M_{obs} Parameter Set (Station Data). The figure compares the best-performing simulated daily flow (dashed red line) against the local observed flow (solid blue line) for the set optimized for the Station Data.

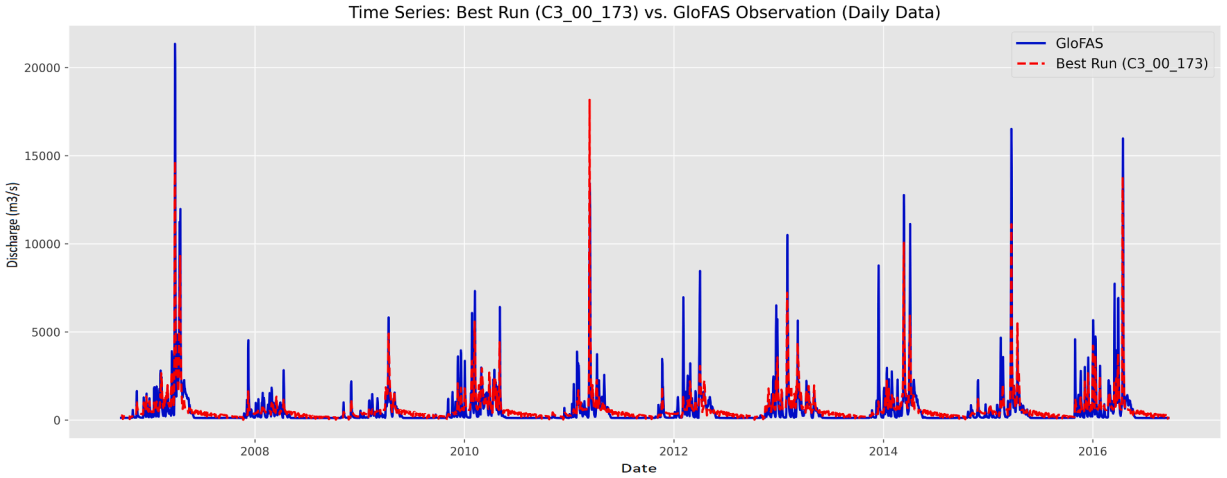

Fig. 6. Simulated vs. Benchmark Time Series for the M_{bench} Parameter Set (GloFAS Data). The figure compares the best-performing simulated daily flow (dashed red line) against the GloFAS benchmark flow (solid blue line) for the set optimized for the GloFAS data.

Table 6
Comparison of statistical performance metrics for the two optimal model sets.

Metric	M_{obs}	M_{bench}
KGE	0.60	0.71
R^2	0.17	0.71
Correlation	0.60	0.85
NSE	0.151	0.71
RMSE	199 $m^3 s^{-1}$	683.3 $m^3 s^{-1}$
MAE	130 $m^3 s^{-1}$	329.4 $m^3 s^{-1}$
Bias	3.95%	11.6%
NSlog	0.098	0.4

reliability and physical consistency.

3.3. Global Sensitivity Analysis and Parameter Interpretability

The SHAP summary plots (Fig. 7) provide a robust physical interpretation of the model's sensitivity. The arnoBeta_add parameter (Infiltration capacity) exhibits the highest magnitude, where high values (red dots) are strongly associated with negative SHAP values.

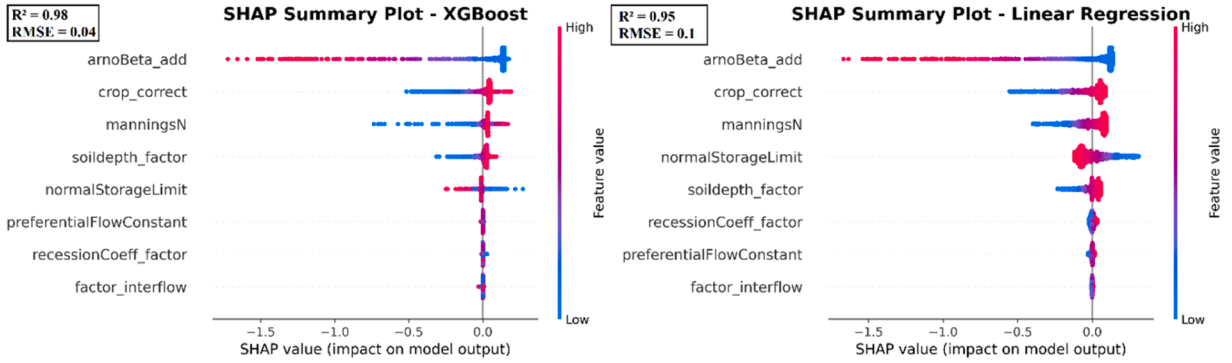

Fig. 7. SHAP Summary Plots for XGBoost (Left) and Linear Regression (Right). The plots quantify the global importance (magnitude) and directional impact (color and position) of the nine calibrated parameters on the model performance (KGE').

Physically, this indicates that excessive infiltration capacity degrades model performance, necessitating a more restricted infiltration rate to generate the surface runoff required to match observed flood peaks. This aligns with the basin's steep topography and complex soil structure, where rapid surface runoff generation during intense precipitation events is a dominant hydrological process.

In contrast, the manningsN (Channel roughness) shows a positive directional impact; higher values (red) contribute to improved model fit. This suggests that the simulated hydrograph requires increased hydraulic residence time to account for the flow attenuation typically induced by the basin's extensive dam infrastructure and the natural complexity of the river network in semi-arid regions. Furthermore, the importance of crop_correct and soildepth_factor highlights the model's high sensitivity to vertical fluxes (evapotranspiration) and storage capacity. The consistency in parameter ranking and direction between the XGBoost and Linear Regression surrogates—despite their different mathematical structures—further validates the hydrological reliability of these sensitivity results.

3.4. Future Hydrological Projections and Computational Framework

This section analyzes the river discharge dynamics projected through the end of the 21st century (2025–2100) using a multi-model, multi-scenario ensemble. The projections integrate the two optimal parameter sets (M_{obs} and M_{bench}) with five GCMs under three Shared Socioeconomic Pathways: SSP1–2.6 (Optimistic), SSP2–4.5 (Average), and SSP5–8.5 (Pessimistic). To capture the temporal evolution of the hydrological cycle, the analysis is segmented into three distinct periods: Near-Future (2025–2050), Mid-Century (2050–2075), and End-of-Century (2075–2100).

The overall trajectory of annual discharge (Fig. 8) reveals a sustained net increase under the Average and Pessimistic scenarios, whereas the Optimistic pathway results in negligible changes or a net reduction. A critical finding is the structural divergence between the two model sets; M_{bench} projections consistently estimate higher absolute magnitudes and greater inter-annual variability compared to the M_{obs} set, which is constrained by regulated station data. This disparity emphasizes that the choice of calibration data fundamentally dictates the projected severity of extremes. While parameter selection influences the baseline, the pronounced GCM spread across both ensembles confirms that climate forcing remains the primary source of uncertainty in inter-annual variability.

Consistent with the previous evaluation of calibration benchmarks, M_{bench} is prioritized for interpreting long-term trends due to its higher physical and statistical reliability. However, the preservation of M_{obs} is essential to establish a necessary uncertainty envelope that accounts for the gap between naturalized flow potential and the constraints of the local observational records. The systematic difference between the two sets is therefore interpreted not as a localized failure, but as a quantified representation of the inherent uncertainties induced by monitoring limitations and anthropogenic data scarcity.

3.4.1. Computational efficiency and ensemble feasibility

The generation of the 30-member projection matrix—encompassing 2250 simulation years—was made feasible by maximizing computational throughput. Initial benchmarking revealed that executing a single 75-year GCM scenario using a standard Python virtual environment (venv) required approximately 11 h. To meet the project's timeline, the framework was transitioned to the UV (Rust-based package manager) environment. This optimization resulted in a 55% increase in execution speed, reducing the processing time to approximately 5 h per run.

3.4.2. Multi-scale analysis of projected changes (Near-Future: 2025–2050)

In the near-future period (2025–2050), the basin exhibits a net increase in mean annual discharge, ranging from 4.4% (SSP5–8.5) to 12.5% (SSP2–4.5) (Table 7). However, these annual trends mask a critical and complex intra-annual redistribution of the hydrological regime. The multi-scale analysis reveals a phenomenon of extreme compression, where the basin concurrently faces significantly higher, earlier flood peaks and intensified late-summer droughts. This explains the apparent contradiction in Table 7, where large negative minimum flow values (e.g., −30.8% under SSP2–4.5) coexist with positive mean annual increases. At the annual resolution, the substantial volumetric contributions from intensified winter and early-spring floods effectively cancel out the severe deficits of the dry season, leading to a misleading net positive change. By contrast, our high-resolution intra-annual assessment successfully identifies

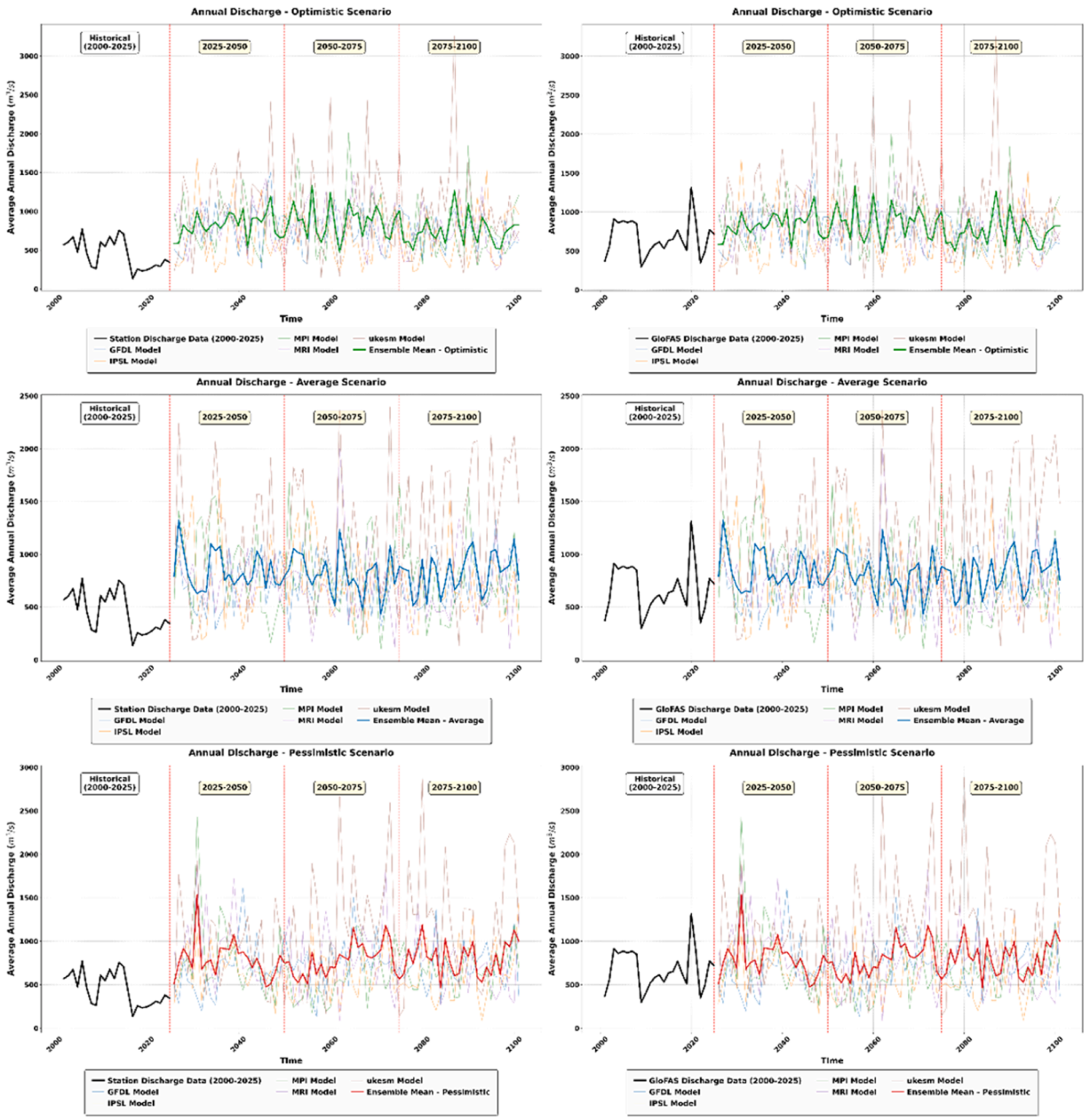

Fig. 8. Comparative Annual Discharge Time Series for M_{obs} (Left) and M_{bench} (Right) Ensembles (2000–2100). The figure illustrates the projected long-term trends and inter-model uncertainty across three SSP scenarios.

these opposing extremes, demonstrating that a stable or increasing annual water yield can still be characterized by devastating seasonal volatility and a simultaneous escalation of both flood and drought risks.

The values reported in Table 7 (and subsequent tables - Table 8 to Table 24) represent the ensemble mean of five GCMs. Specifically, the maximum, minimum, and mean metrics for each period are calculated by averaging the respective yearly extreme values across the entire 5-member GCM ensemble for the 25-year duration; therefore, these figures do not represent isolated, individual extreme events, but rather the collective trend projected by the ensemble.

3.4.2.1. Seasonal and monthly shifts. A consistent increase in cold-season flow is observed, with Winter and Spring mean discharge rising by up to 32.6% and 32.1%, respectively (Table 8). This hydrograph advancement is linked to rising air temperatures (Fig. 9 and Fig. 10), which shift precipitation from snow to rain and accelerate snowmelt timing. Monthly breakdowns confirm that March (68.3%) and February (50.0%) experience the highest increases, often driven by extreme, early-season flood events (Supplementary Fig. 33 and Fig. 37). Conversely, Summer and Autumn face a significant drying trend, with mean reductions reaching −27.2%

Table 7
Multi-scale summary of projected percentage change (%) in Mean, Maximum (Max), and Minimum (Min) Flow (M_{obs}) for the near-future period (2025–2050). The background color indicates flow magnitude: Red tones signify higher increases or lower decreases, and green tones signify lower increases or higher decreases.

Scenario	Optimistic (SSP1-2.6)			Average (SSP2-4.5)			Pessimistic (SSP5-8.5)		
Time Period	Mean%	Max%	Min%	Mean%	Max%	Min%	Mean%	Max%	Min%
Daily	12.4	199.0	24.4	14.2	123.5	-30.8	6.0	241.1	24.7
Monthly	8.4	88.0	-48.1	10.2	61.9	-69.7	2.2	107.4	-48.2
Seasonal	8.6	53.6	-34.7	10.6	74.7	-59.6	2.6	64.8	-38.7
Annual	10.7	31.5	-11.6	12.5	26.1	-27.9	4.4	38.7	-21.0

Table 8
Seasonal summary of projected percentage change (%) in Mean, Maximum (Max), and Minimum (Min) Flow (M_{obs}) for the Near-Future Period (2025–2050). The background color indicates flow magnitude: Red tones signify higher increases or lower decreases, and green tones signify lower increases or higher decreases.

Scenario	Optimistic (SSP1-2.6)			Average (SSP2-4.5)			Pessimistic (SSP5-8.5)		
Season	Mean%	Max%	Min%	Mean%	Max%	Min%	Mean%	Max%	Min%
Winter	32.6	227.5	84.7	32.2	212.5	55.1	25.9	363.3	57.1
Spring	22.3	131.3	8.4	32.1	100.6	-14.5	10.8	104.5	7.4
Summer	-10.0	-31.7	-19.8	-9.0	-32.9	-66.3	-12.7	-23.7	-36.0
Autumn	-18.0	930.8	3.9	-27.2	273.5	-45.2	-17.8	545.4	-3.0

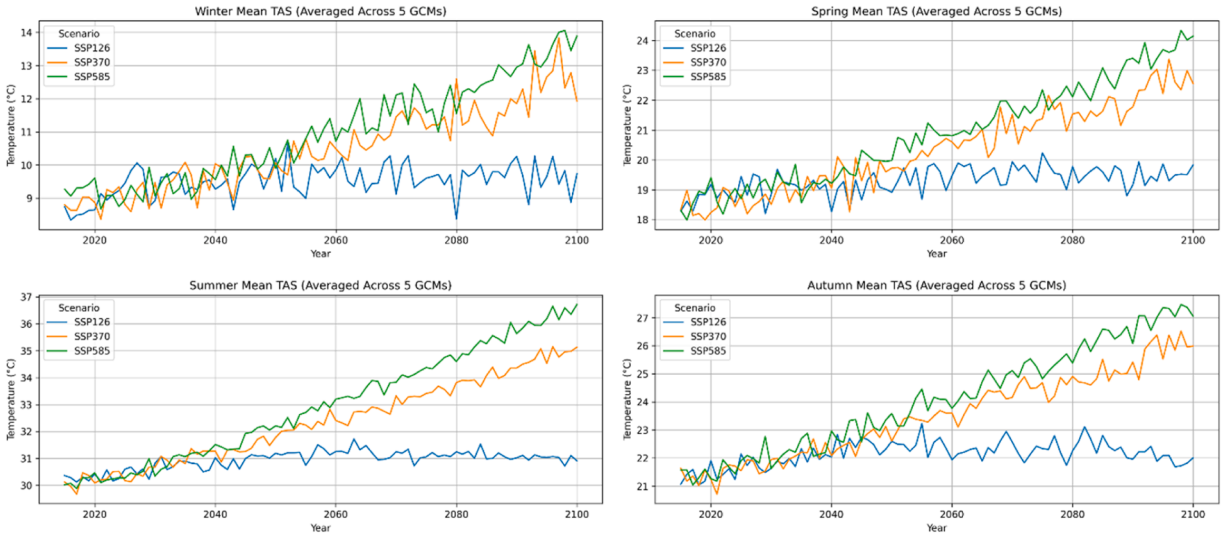

Fig. 9. Projected Seasonal Mean Surface Air Temperature (TAS) Trend Averaged Across Five GCMs (2015–2100). The figure illustrates the long-term changes in mean Seasonal temperature (°C) across the three Shared Socioeconomic Pathway (SSP) scenarios.

(Table 7). The intensification of summer drought (e.g., −66.3% in August in Table 9) is visually supported by the ensemble boxplots, showing a notable downward shift in discharge medians compared to historical observations (Fig. 11 & Fig. 12; Supplementary Fig. 34 and Fig. 38).

3.4.2.2. Hydrological extremes. Daily scale analysis reveals an alarming increase in fluvial flood risk, with maximum daily flows (Max

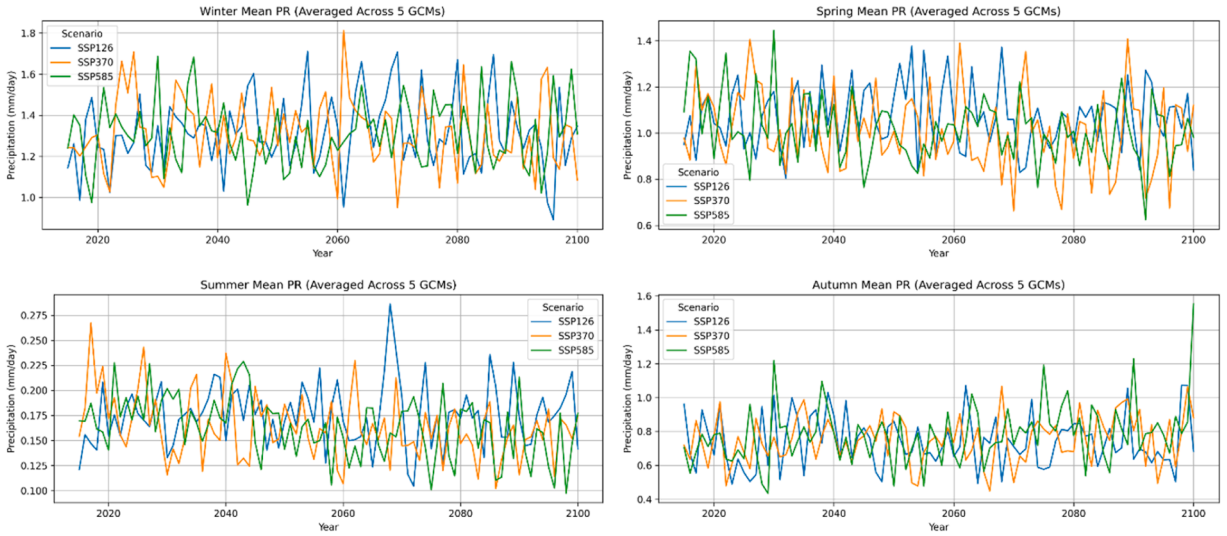

Fig. 10. Projected Seasonal Mean Precipitation (PR) Trend Averaged Across Five GCMs (2015–2100). The figure illustrates the long-term changes in mean Seasonal Precipitation (mm/day) across the three Shared Socioeconomic Pathway (SSP) scenarios.

Table 9
Monthly summary of projected percentage change (%) in Mean, Maximum (Max), and Minimum (Min) Flow (M_{obs}) for the Near-Future Period (2025–2050). The background color indicates flow magnitude: Red tones signify higher increases or lower decreases, and green tones signify lower increases or higher decreases.

Scenario	Optimistic (SSP1-2.6)			Average (SSP2-4.5)			Pessimistic (SSP5-8.5)		
Month	Mean%	Max%	Min%	Mean%	Max%	Min%	Mean%	Max%	Min%
January	17.7	109.7	117.5	26.4	157.9	66.8	16.3	113.0	146.9
February	40.6	139.6	60.9	50.0	160.9	5.2	29.6	82.7	18.2
March	57.7	117.6	42.6	68.3	133.9	19.5	35.2	110.8	28.8
April	8.2	81.3	17.0	25.7	73.8	-4.4	2.5	26.7	20.8
May	2.6	121.6	-13.1	1.1	39.9	-25.6	-4.7	46.1	-0.7
June	3.6	-24.1	-16.2	4.9	-25.4	-34.1	1.4	-15.2	-13.8
July	-12.6	-46.4	-25.7	-11.2	-46.5	-50.3	-15.1	-43.4	-34.4
August	-21.6	-56.7	-19.8	-21.4	-56.7	-66.3	-25.0	-55.4	-36.0
September	-22.5	-61.0	-23.1	-22.8	-61.6	-64.2	-25.9	-59.2	-29.4
October	-32.5	-52.9	-19.1	-31.4	-22.1	-55.6	-34.3	109.7	-28.3
November	-1.8	930.8	14.6	-27.7	273.5	-18.7	3.5	545.4	11.7
December	42.2	183.9	-18.6	20.4	98.0	-32.1	33.7	282.0	-31.6

%) surging by up to 241.1% (Table 7). This amplification of extremes is further detailed in the daily discharge distribution boxplots (Supplementary Fig. 2). While cold-season baseflow stabilizes due to increased liquid precipitation, the warm season remains vulnerable to severe deficits, interspersed with isolated flash flood spikes in Autumn (Fig. 10).

3.4.2.3. Model Coherence and Uncertainty (M_{obs} vs M_{bench}). Projections from both M_{obs} and M_{bench} are highly synchronized regarding the timing of seasonal shifts, providing high confidence in the climate signal (Table 10, Table 11, and Table 12 for M_{bench}). However, M_{bench} consistently estimates higher absolute magnitudes and exhibits a wider uncertainty envelope across the ensemble distribution (Supplementary Fig. 16 to Fig 19). This discrepancy highlights the structural uncertainty where M_{obs} is conditioned by regulated station data, while M_{bench} reflects a more naturalized flow regime.

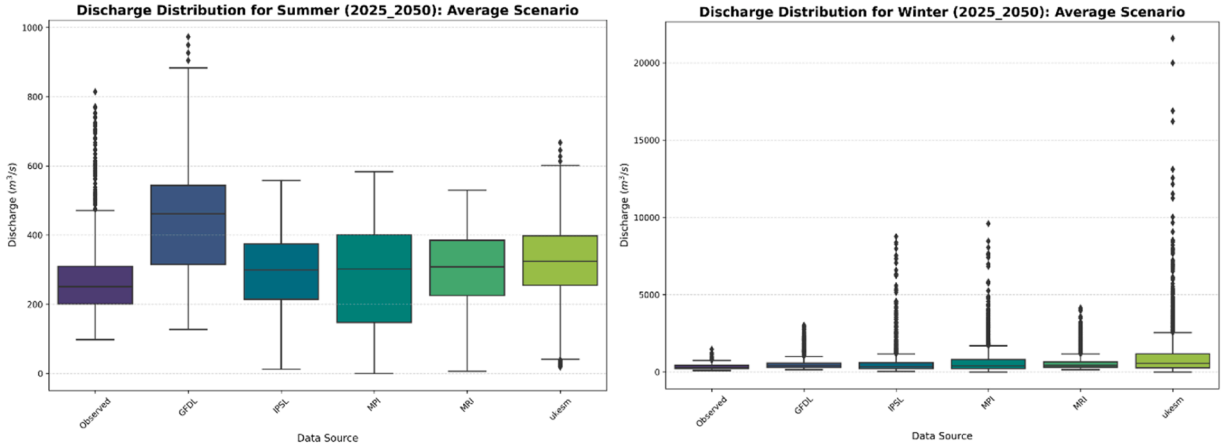

Fig. 11. Inter-Model Uncertainty in Seasonal Discharge Distribution (M_{obs} Ensemble) for the Near-Future Period (2025–2050). The boxplots illustrate the distribution of seasonal mean discharge projected by the ensemble of five GCMs for selected seasons and scenarios in relation to the Observed flow. Full seasonal boxplots for all three SSP scenarios are detailed in Supplementary Fig. 3.

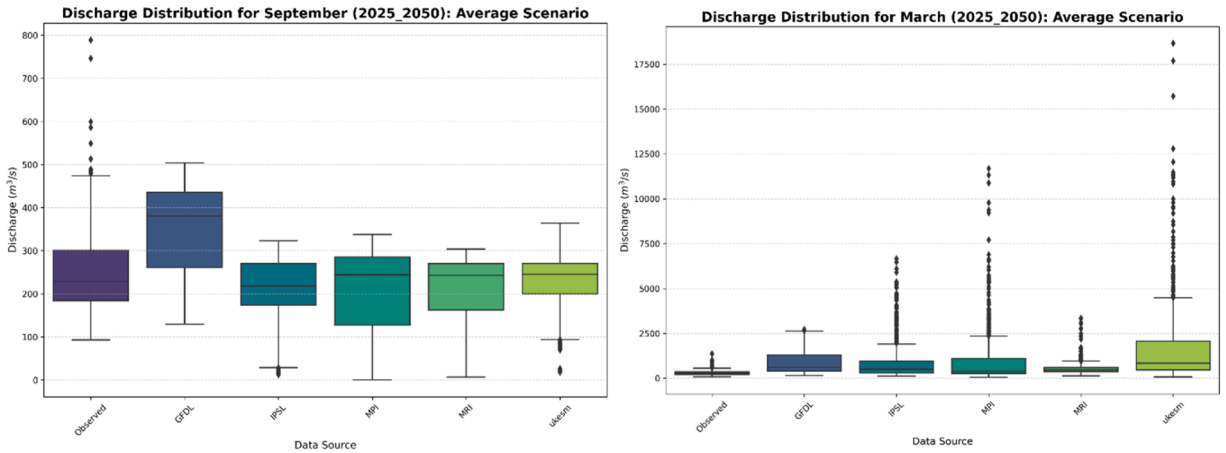

Fig. 12. Inter-Model Uncertainty in Monthly Discharge Distribution (M_{obs} Ensemble) for the Near-Future Period (2025–2050). The boxplots illustrate the distribution of monthly mean discharge projected by the ensemble of five GCMs for selected months and scenarios in relation to the Observed flow. Full monthly boxplots for all three SSP scenarios are detailed in Supplementary Fig. 4 and Fig. 5.

Table 10
Multi-Scale Summary of Projected Percentage Change (%) in Mean, Maximum (Max), and Minimum (Min) Flow (M_{bench}) for the Near-Future Period (2025–2050). The background color indicates flow magnitude: Red tones signify higher increases or lower decreases, and green tones signify lower increases or higher decreases.

Scenario	Optimistic (SSP1-2.6)			Average (SSP2-4.5)			Pessimistic (SSP5-8.5)		
Time Period	Mean%	Max%	Min%	Mean%	Max%	Min%	Mean%	Max%	Min%
Daily	22.3	22.6	-89.0	24.3	8.4	-90.2	17.2	29.6	-90.8
Monthly	22.4	67.8	-11.1	24.3	64.2	-40.2	17.2	85.1	-23.5
Seasonal	23.3	20.4	11.8	26.0	39.6	-20.9	18.4	26.8	-5.1
Annual	22.4	28.3	-7.7	24.3	18.7	-16.1	17.2	35.8	-14.1

Table 11
Seasonal summary of projected percentage change (%) in Mean, Maximum (Max), and Minimum (Min) Flow (M_{bench}) for the Near-Future Period (2025–2050). The background color indicates flow magnitude: Red tones signify higher increases or lower decreases, and green tones signify lower increases or higher decreases.

Scenario	Optimistic (SSP1-2.6)			Average (SSP2-4.5)			Pessimistic (SSP5-8.5)		
Season	Mean%	Max%	Min%	Mean%	Max%	Min%	Mean%	Max%	Min%
Winter	29.9	30.6	-80.2	32.1	64.1	-82.9	24.0	105.2	-83.0
Spring	-1.8	6.3	-19.5	4.3	-7.6	-42.6	-6.7	-11.9	-18.2
Summer	150.6	-36.6	-70.5	151.7	-45.6	-89.2	148.7	-37.2	-72.6
Autumn	66.2	132.3	-89.0	42.5	18.9	-88	61.6	50.0	-90.3

Table 12
Monthly summary of projected percentage change (%) in Mean, Maximum (Max), and Minimum (Min) Flow (M_{bench}) for the Near-Future Period (2025–2050). The background color indicates flow magnitude: Red tones signify higher increases or lower decreases, and green tones signify lower increases or higher decreases.

Scenario	Optimistic (SSP1-2.6)			Average (SSP2-4.5)			Pessimistic (SSP5-8.5)		
Month	Mean%	Max%	Min%	Mean%	Max%	Min%	Mean%	Max%	Min%
January	24.1	18.8	-68.7	40.7	80.9	-47.3	28.0	51.6	-70.8
February	27.5	21.7	-65.2	30.6	14.0	-50.0	16.0	14.6	-52.3
March	11.2	-8.9	-21.6	15.8	-15.3	-31.4	-0.2	-17.2	-22.3
April	-20.4	50.0	51.1	-9.5	50.7	-16.0	-20.0	5.5	11.2
May	11.7	47.9	11.9	8.5	29.0	-10.3	11.4	47.1	14.1
June	188.4	-36.6	-15.7	189.6	-45.6	-57.4	186.7	-37.2	-37.7
July	152.6	312.9	-50.4	153.4	312.5	-81.0	150.1	316.2	-63.9
August	106.3	219.0	-70.5	107.6	225.4	-88.2	104.7	231.4	-71.4
September	87.8	15.2	-72.6	88.5	17.8	-83.9	85.8	18.8	-82.4
October	35.4	-75.4	-82.7	51.4	-50.1	-87.7	56.1	60.8	-89.2
November	70.7	132.3	-88.1	25.7	16.6	-86.7	56.3	50.0	-84.8
December	39.5	43.0	-65.4	24.2	48.0	-66.0	29.4	190.9	-82.3

3.4.3. Multi-Scale Analysis of Projected Changes (Mid-Century: 2050–2075)

Projections for the mid-century period (2050–2075) indicate a clear intensification of the hydrological shifts observed in the near-future, with higher magnitudes of change and increased scenario divergence (Table 13). At the annual scale, all scenarios maintain a net positive change in mean discharge, peaking at 18.1% (SSP1–2.6). This increase is primarily attributed to higher annual precipitation offsetting enhanced evaporative losses (Supplementary Fig. 31 and Fig. 35). However, the range between the maximum (36.9%) and minimum (-51.6%) projected annual changes highlights a significantly wider uncertainty envelope compared to the previous period.

3.4.3.1. Seasonal and monthly shifts. The seasonal hydrograph shows a severe exacerbation of the shift toward cold-season flow. In Table 14, Winter discharge mean increases reach 47.6% (SSP2–4.5), driven by a near-complete transition from snow to rain and accelerated spring melt caused by rising air temperatures (Fig. 9 and Fig. 10). Peak monthly flows continue to advance, with March and February showing increases up to 76.5% (Table 15), a trend visually detailed in the ensemble distributions (Supplementary Fig. 33 and Fig. 37). Conversely, the warm-season drying trend is markedly amplified; mean reductions in Autumn reach −39.5% (October, SSP5–8.5), signifying early exhaustion of soil moisture reservoirs and increased evaporative demand.

3.4.3.2. Hydrological extremes. Daily scale analysis reveals an alarming amplification of hydrological risks (Table 13). Maximum daily flows (Max%) are projected to increase by up to 213.1% (SSP2–4.5), a shift reflected in the extended whiskers and outliers of the winter boxplots (Fig. 13). More critically, the risk of baseflow failure becomes catastrophic under the pessimistic scenario (SSP5–8.5), with

Table 13
Multi-scale summary of projected percentage change (%) in Mean, Maximum (Max), and Minimum (Min) Flow (M_{obs}) for the Mid-Century Period (2050–2075). The background color indicates flow magnitude: Red tones signify higher increases or lower decreases, and green tones signify lower increases or higher decreases.

Scenario	Optimistic (SSP1-2.6)			Average (SSP2-4.5)			Pessimistic (SSP5-8.5)		
Time Period	Mean%	Max%	Min%	Mean%	Max%	Min%	Mean%	Max%	Min%
Daily	19.8	147.9	3.9	13.2	213.1	-10.0	8.1	131.9	-97.9
Monthly	15.7	88.1	-57.4	9.0	97.5	-62.8	4.3	70.2	-98.5
Seasonal	16.1	64.2	-46.8	10.0	95.9	-55.2	4.8	51.2	-89.3
Annual	18.1	36.9	-17.8	11.5	34.9	-23.5	6.5	25.2	-51.6

Table 14
Seasonal Summary of Projected Percentage Change (%) in Mean, Maximum (Max), and Minimum (Min) Flow (M_{obs}) for the Mid-Century Period (2050–2075). The background color indicates flow magnitude: Red tones signify higher increases or lower decreases, and green tones signify lower increases or higher decreases.

Scenario	Optimistic (SSP1-2.6)			Average (SSP2-4.5)			Pessimistic (SSP5-8.5)		
Season	Mean%	Max%	Min%	Mean%	Max%	Min%	Mean%	Max%	Min%
Winter	43.8	218.6	74.4	47.6	351.0	44.3	45.5	214.6	-36.7
Spring	35.3	99.3	16.7	18.4	144.5	2.6	10.7	86.6	-49.9
Summer	-8.5	-31.3	-47.5	-13.2	-38.8	-50.4	-19.3	-35.1	-91.9
Autumn	-20.6	478.7	-16.3	-25.6	286.7	-31.5	-29.0	436.1	-98.4

Table 15
Monthly Summary of Projected Percentage Change (%) in Mean, Maximum (Max), and Minimum (Min) Flow (M_{obs}) for the Mid-Century Period (2050–2075). The background color indicates flow magnitude: Red tones signify higher increases or lower decreases, and green tones signify lower increases or higher decreases.

Scenario	Optimistic (SSP1-2.6)			Average (SSP2-4.5)			Pessimistic (SSP5-8.5)		
Month	Mean%	Max%	Min%	Mean%	Max%	Min%	Mean%	Max%	Min%
January	35.4	170.7	141.1	44.6	236.2	179.3	38.9	166.1	60.3
February	71.6	195.7	36.6	33.8	101.3	51.3	54.1	127.7	-0.3
March	76.5	150.9	61.3	58.1	133.1	66.3	48.7	117.0	-16.5
April	24.0	33.6	15.3	3.9	103.0	20.8	-4.6	29.5	-44.0
May	5.4	76.7	-7.8	-5.5	12.1	-18.9	-10.4	46.0	-60.4
June	5.6	-23.6	-15.2	0.5	-32.0	-30.9	-6.7	-27.9	-71.6
July	-10.8	-45.7	-36.9	-15.5	-48.5	-46.7	-21.4	-47.5	-84.4
August	-20.9	-56.4	-47.4	-25.3	-58.7	-50.4	-30.2	-57.9	-91.9
September	-22.4	-60.6	-41.6	-26.6	-63.3	-48.1	-31.2	-62.2	-97.0
October	-32.9	-44.8	-35.6	-36.0	-54.6	-54.9	-39.5	-36.4	-99.1
November	-8.7	477.9	8.4	-15.8	286.7	-27.0	-18.1	436.1	-96.0
December	24.3	77.8	-23.6	66.2	376.0	-37.2	44.6	186.3	-71.6

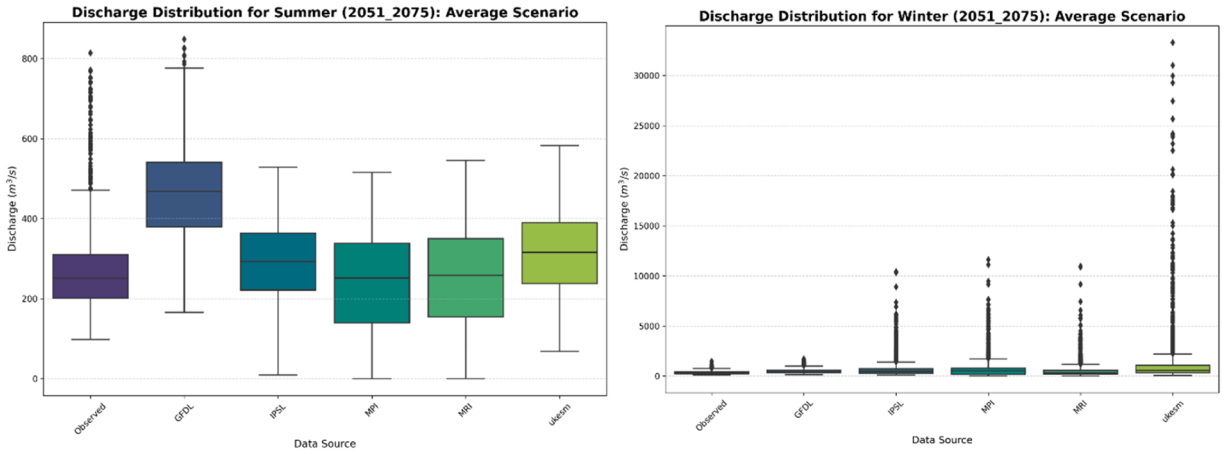

Fig. 13. Inter-Model Uncertainty in Seasonal Discharge Distribution (M_{obs} Ensemble) for the Mid-Century Period (2050–2075). The boxplots illustrate the distribution of seasonal mean discharge projected by the ensemble of five GCMs for selected seasons and scenarios in relation to the Observed flow. Full seasonal boxplots for all three SSP scenarios are detailed in Supplementary Fig. 8.

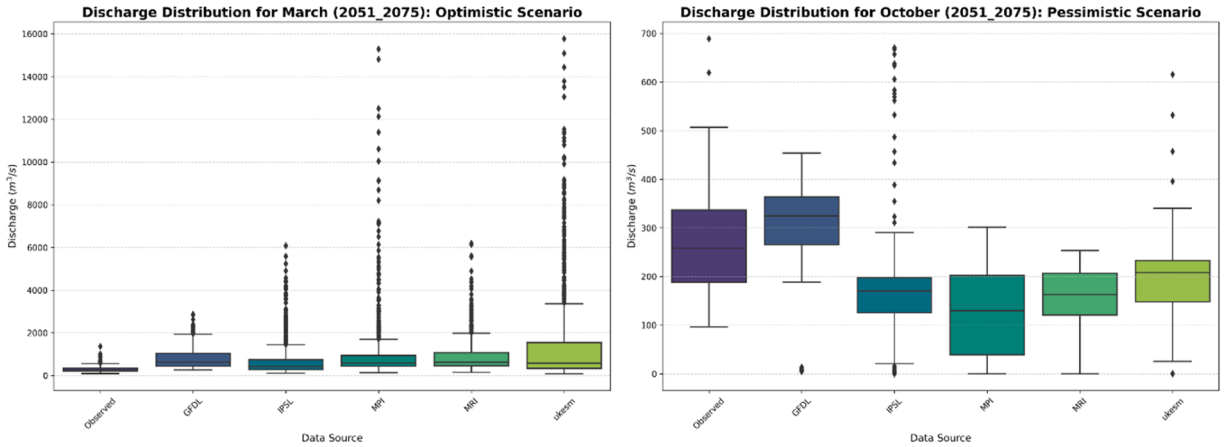

Fig. 14. Inter-Model Uncertainty in Monthly Discharge Distribution (M_{obs} Ensemble) for the Mid-Century Period (2050–2075). The boxplots illustrate the distribution of monthly mean discharge projected by the ensemble of five GCMs for selected months and scenarios in relation to the Observed flow. Full monthly boxplots for all three SSP scenarios are detailed in Supplementary Fig. 9 and Fig. 10.

minimum daily flows decreasing by −97.9%. This potential for near-total baseflow collapse in October and September is visually anchored in the ensemble spreads (Fig. 14) and the severe monthly reduction trends in the supplementary data (Supplementary Fig. 34 and Fig. 38).

Table 16
Multi-scale summary of projected percentage change (%) in Mean, Maximum (Max), and Minimum (Min) Flow (M_{bench}) for the Mid-Century Period (2050–2075). The background color indicates flow magnitude: Red tones signify higher increases or lower decreases, and green tones signify lower increases or higher decreases.

Scenario	Optimistic (SSP1-2.6)			Average (SSP2-4.5)			Pessimistic (SSP5-8.5)		
Time Period	Mean%	Max%	Min%	Mean%	Max%	Min%	Mean%	Max%	Min%
Daily	28.34	10.16	-88.98	21.00	30.33	-93.19	15.08	15.19	-98.67
Monthly	28.49	75.36	-37.91	20.83	79.62	-55.36	15.21	53.72	-91.94
Seasonal	29.70	35.08	-15.79	23.07	44.40	-42.25	16.18	24.64	-82.65
Annual	28.35	30.16	-8.12	21.00	32.34	-31.00	15.08	27.48	-50.69

Table 17
Seasonal summary of projected percentage change (%) in Mean, Maximum (Max), and Minimum (Min) Flow (M_{bench}) for the Mid-Century Period (2050–2075). The background color indicates flow magnitude: Red tones signify higher increases or lower decreases, and green tones signify lower increases or higher decreases.

Scenario	Optimistic (SSP1-2.6)			Average (SSP2-4.5)			Pessimistic (SSP5-8.5)		
Season	Mean%	Max%	Min%	Mean%	Max%	Min%	Mean%	Max%	Min%
Winter	40.5	66.0	-85.8	40.4	108.2	-84.3	36.7	86.2	-89.5
Spring	4.5	-13.5	-15.7	-8.3	9.2	-38.2	-15.8	-12.9	-93.3
Summer	148.7	-47.7	-80.9	141.1	-32.5	-88.6	124.8	-45.3	-97.6
Autumn	54.3	45.2	-87.8	48.7	12.2	-90.7	48.5	61.4	-97.0

Table 18
Monthly Summary of Projected Percentage Change (%) in Mean, Maximum (Max), and Minimum (Min) Flow (M_{bench}) for the Mid-Century Period (2050–2075). The background color indicates flow magnitude: Red tones signify higher increases or lower decreases, and green tones signify lower increases or higher decreases.

Scenario	Optimistic (SSP1-2.6)			Average (SSP2-4.5)			Pessimistic (SSP5-8.5)		
Month	Mean%	Max%	Min%	Mean%	Max%	Min%	Mean%	Max%	Min%
January	43.0	66.0	-61.6	43.1	57.1	-66.9	30.4	49.0	-80.4
February	47.8	61.1	-8.2	19.5	7.1	-46.8	35.9	54.5	-81.4
March	18.5	-15.2	-4.3	6.5	-3.2	-17.8	-5.9	-21.9	-91.1
April	-14.0	28.1	23.5	-29.4	48.5	-31.4	-32.1	30.4	-84.1
May	14.7	94.6	-9.1	6.7	-7.5	-35.7	0.6	43.8	-88.8
June	186.1	-47.7	-58.2	179.1	-32.5	-69.1	161.1	-45.3	-95.1
July	150.4	308.0	-78.4	141.2	313.5	-87.0	124.5	306.2	-97.1
August	105.2	218.9	-78.6	98.4	217.2	-88.2	84.4	209.4	-97.5
September	86.9	15.0	-81.2	79.7	17.9	-89.3	71.6	56.4	-96.5
October	36.4	-64.0	-86.6	37.9	-42.4	-89.1	36.0	-27.8	-96.6
November	50.9	45.2	-86.0	43.4	12.2	-89.6	46.1	61.4	-92.2
December	28.3	58.4	-82.4	64.0	220.9	-82.1	44.9	146.3	-70.6

Table 19
Multi-scale summary of projected percentage change (%) in Mean, Maximum (Max), and Minimum (Min) Flow (M_{obs}) for the End-of-Century Period (2075–2100). The background color indicates flow magnitude: Red tones signify higher increases or lower decreases, and green tones signify lower increases or higher decreases.

Scenario	Optimistic (SSP1-2.6)			Average (SSP2-4.5)			Pessimistic (SSP5-8.5)		
Time Period	Mean%	Max%	Min%	Mean%	Max%	Min%	Mean%	Max%	Min%
Daily	0.4	163.5	3.1	17.4	227.6	-17.8	16.0	317.6	-4.9
Monthly	-3.1	120.7	-55.0	13.3	88.7	-66.6	11.9	112.8	-56.6
Seasonal	-2.6	86.3	-37.8	14.0	71.4	-56.3	13.6	91.8	-47.7
Annual	-1.1	46.2	-14.9	15.7	22.1	-20.5	14.3	30.2	-16.5

3.4.3.3. Model coherence and uncertainty (M_{obs} vs M_{bench}). Each parameter sets remain qualitatively synchronized on the direction of change, reinforcing the climate signal. However, significant magnitude differences exist; for instance, M_{obs} projects a 6.5% annual increase under SSP5–8.5, while M_{bench} estimates a higher 15.08% (Table 16, Table 17, and Table 18). The structural uncertainty inherited from the calibration data is evident in the distinct distribution shapes and interquartile ranges (IQR) of M_{bench} compared to M_{obs} (Supplementary Fig. 21 to Fig. 25), emphasizing how the choice of benchmark impacts the projected uncertainty envelope.

3.4.4. Multi-scale analysis of projected changes (End-of-Century: 2075–2100)

The hydrological projections for the late 21st century (2075–2100) reveal a definitive divergence in the basin's water budget. While the Average and Pessimistic scenarios (SSP2–4.5 and SSP5–8.5) project continued annual flow increases of 15.7% and 14.3%, respectively, the Optimistic scenario (SSP1–2.6) indicates a net reduction of −1.1% (Table 19). This shift suggests that under low-emissions pathways, rising thermal forcing and evaporative demand may eventually offset precipitation gains, leading to a long-term water deficit (Supplementary Fig. 31 and Fig. 35).

3.4.4.1. Seasonal and monthly shifts. The temporal redistribution of flow reaches its peak intensification in this period. Winter discharge dominates the hydrograph with mean increases of up to 67.8% (SSP2–4.5), driven by the near-total transition to a rainfall-dominated regime (Fig. 9 and Fig. 10). This cold-season concentration is visually confirmed by the upward shift of ensemble medians and the presence of extreme outliers in December and January (Fig. 15 and Fig. 16). Conversely, Autumn and Summer face widespread declines (up to −29.8% in Table 20), with a pronounced risk of multi-month hydrological drought. Most notably, Autumn maximum flows exhibit a "catastrophic destabilization," with storm-driven spikes reaching 887.2% (SSP5–8.5). This volatile pattern—long periods of near-zero flow interrupted by extreme flash floods—is anchored in the ensemble boxplots for November and October (Table 21, Supplementary Fig. 34 and Fig. 38).

3.4.4.2. Hydrological extremes. Daily scale analysis (Table 19) confirms that the flow regime will be defined by fewer, but exceptionally intense, high-flow events. The maximum daily flow (Max%) is projected to surge by a severe 317.6% (SSP5–8.5), a trend further detailed in the end-century daily distribution boxplots (Supplementary Fig 12). While baseflow may marginally stabilize under the optimistic scenario, the Average scenario projects a −17.8% reduction in daily minimum flow, signaling critical groundwater depletion during dry periods.

3.4.4.3. Model coherence and uncertainty (M_{obs} vs M_{bench}). Comparison with the M_{bench} ensemble (Table 22, Table 23, and Table 24) reveals persistent structural uncertainty. While both configurations agree on the amplification of extremes, M_{bench} exhibits a consistently smaller interquartile range (IQR) and different distribution shapes compared to M_{obs} (Supplementary Fig 26 to Fig. 30). The most striking divergence occurs in Autumn flood peaks, where M_{obs} projects magnitudes an order of magnitude higher than M_{bench}, underscoring how calibration data selection significantly impacts the assessment of high-end climate risks and infrastructure planning by the end of the century.

3.4.5. Analysis of Extreme Flow Amplification and Climatic Drivers

To establish the physical justification for the projected increase in flood magnitudes (Max%), the relationship between climatic forcing and hydrological response was evaluated using normalized maximum daily precipitation and streamflow (Fig. 17). The analysis confirms a direct positive correlation across all scenarios, indicating that the intensification of flood events is primarily driven by the increased frequency and intensity of extreme rainfall.

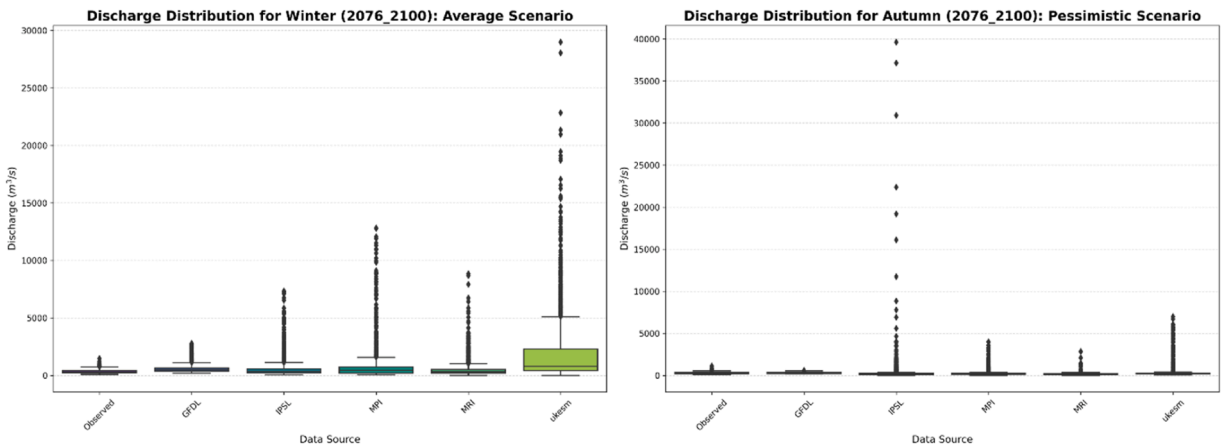

Fig. 15. Inter-Model Uncertainty in Seasonal Discharge Distribution (M_{obs} Ensemble) for the End-of-Century Period (2075–2100). The boxplots illustrate the distribution of seasonal mean discharge projected by the ensemble of five GCMs for selected seasons and scenarios in relation to the Observed flow. Full seasonal boxplots for all three SSP scenarios are detailed in Supplementary Fig. 13.

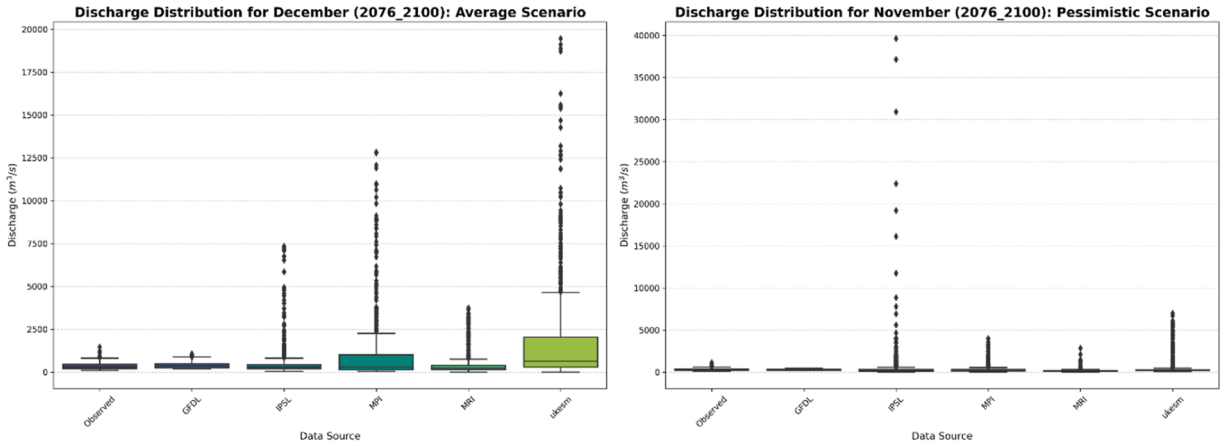

Fig. 16. Inter-Model Uncertainty in Monthly Discharge Distribution (M_{obs} Ensemble) for the End-of-Century Period (2075–2100). The boxplots illustrate the distribution of monthly mean discharge projected by the ensemble of five GCMs for selected months and scenarios in relation to the Observed flow. Full monthly boxplots for all three SSP scenarios are detailed in Supplementary Fig. 14 and Fig. 15.

Table 20
Seasonal Summary of Projected Percentage Change (%) in Mean, Maximum (Max), and Minimum (Min) Flow (M_{obs}) for the End-of-Century Period (2075–2100). The background color indicates flow magnitude: Red tones signify higher increases or lower decreases, and green tones signify lower increases or higher decreases.

Scenario	Optimistic (SSP1-2.6)			Average (SSP2-4.5)			Pessimistic (SSP5-8.5)		
Season	Mean%	Max%	Min%	Mean%	Max%	Min%	Mean%	Max%	Min%
Winter	14.7	290.8	9.0	67.8	303.0	26.9	63.5	341.6	101.0
Spring	10.9	93.4	19.4	14.5	157.2	17.7	12.7	87.1	11.3
Summer	-14.5	-35.7	-30.0	-17.9	-33.7	-51.8	-18.6	-33.2	-39.4
Autumn	-29.8	230.1	-5.5	-21.0	751.3	-37.6	-18.0	887.2	-27.2

A critical finding is the escalating sensitivity of the basin's response proportional to the severity of climate forcing. The Coefficient of Determination (R^2), which quantifies the influence of precipitation on streamflow variance, increases significantly from 0.102 (SSP1–2.6) to 0.345 (SSP5–8.5). This progressive strengthening of the R^2 value suggests that under higher emission pathways, the basin's hydrological system becomes more directly responsive to extreme precipitation. This thermodynamic intensification of the water cycle—where precipitation is delivered in fewer but more intense events—is the dominant mechanism driving the catastrophic flood risks identified in the high-emission projections.

4. Discussion and suggestions

4.1. The accelerated hydrological cycle: From snow to immediate runoff

The primary driver of hydrological transformation in these basins is the unwavering warming trend projected across all SSPs (Supplementary Fig. 31 to Fig. 34). In regions with high elevation and semi-arid conditions—similar to this study area—the snowpack traditionally functions as a natural reservoir. Our findings confirm that higher winter temperatures transform this delayed release mechanism into premature runoff, a phenomenon termed the early-spring runoff effect.

This projected hydrograph transformation, characterized by a shift in peak flows from late spring to late winter, mirrors the trends observed in other snow-dependent global basins. For instance, the observed advancement in peak runoff timing aligns with the 15–30-day shifts reported in the Himalayas (Iqbal et al., 2022) and the seasonal shifts documented in the Rocky Mountains (Zareian and Salem, 2022). Furthermore, the reduction in seasonal snow storage in the Karun-Karkheh-Marzi-e-Gharb complex is consistent with the extensive snowpack declines (up to 50%) documented across the European Alps (Matiu et al., 2021). This directional alignment confirms that the basin is undergoing a thermal-driven hydrological shift (Yao et al., 2023) that is physically consistent with the patterns observed in major high-altitude regions worldwide.

Table 21
Monthly Summary of Projected Percentage Change (%) in Mean, Maximum (Max), and Minimum (Min) Flow (M_{obs}) for the End-of-Century Period (2075–2100). The background color indicates flow magnitude: Red tones signify higher increases or lower decreases, and green tones signify lower increases or higher decreases.

Scenario	Optimistic (SSP1-2.6)			Average (SSP2-4.5)			Pessimistic (SSP5-8.5)		
Month	Mean%	Max%	Min%	Mean%	Max%	Min%	Mean%	Max%	Min%
January	12.1	307.9	85.3	55.2	306.3	135.4	64.0	249.4	114.4
February	32.2	185.0	44.6	65.0	140.9	67.7	51.5	95.5	75.7
March	31.0	58.2	54.3	46.3	222.6	46.9	50.1	122.8	55.5
April	8.5	77.1	11.5	2.8	9.3	17.4	0.5	13.2	2.0
May	-7.8	31.1	-4.5	-4.6	96.9	3.6	-11.7	7.5	-10.8
June	-1.6	-28.5	-11.6	-4.9	-26.3	-11.2	-5.2	-25.8	-21.8
July	-16.7	-47.4	-22.2	-20.2	-47.1	-42.7	-20.8	-47.4	-41.5
August	-25.8	-57.6	-30.0	-29.4	-57.1	-51.8	-30.2	-57.8	-39.2
September	-26.5	-62.3	-32.8	-29.8	-61.4	-53.3	-30.4	-61.4	-37.3
October	-36.2	-56.1	-43.0	-30.4	323.8	-61.7	-35.9	92.3	-47.9
November	-27.3	230.1	-4.5	-5.5	548.7	-37.6	8.1	885.4	-22.3
December	-0.7	48.6	-49.3	86.3	211.1	-44.8	76.1	317.8	-12.4

Table 22
Multi-scale summary of projected percentage change (%) in Mean, Maximum (Max), and Minimum (Min) Flow (M_{bench}) for the End-of-Century Period (2075–2100). The background color indicates flow magnitude: Red tones signify higher increases or lower decreases, and green tones signify lower increases or higher decreases.

Scenario	Optimistic (SSP1-2.6)			Average (SSP2-4.5)			Pessimistic (SSP5-8.5)		
Time Period	Mean%	Max%	Min%	Mean%	Max%	Min%	Mean%	Max%	Min%
Daily	11.93	17.26	-88.88	21.95	32.77	-95.83	21.51	54.52	-92.68
Monthly	11.94	83.42	-11.05	21.86	68.42	-63.62	21.38	95.99	-41.19
Seasonal	13.47	48.98	7.25	23.37	36.95	-43.46	24.12	43.41	-18.49
Annual	11.94	37.08	-11.07	21.96	21.12	-20.95	21.51	26.71	-8.59

Table 23
Seasonal summary of projected percentage change (%) in Mean, Maximum (Max), and Minimum (Min) Flow (M_{bench}) for the End-of-Century Period (2075–2100). The background color indicates flow magnitude: Red tones signify higher increases or lower decreases, and green tones signify lower increases or higher decreases.

Scenario	Optimistic (SSP1-2.6)			Average (SSP2-4.5)			Pessimistic (SSP5-8.5)		
Season	Mean%	Max%	Min%	Mean%	Max%	Min%	Mean%	Max%	Min%
Winter	13.6	80.5	-78.8	46.3	86.5	-90.9	51.7	107.3	-83.3
Spring	-5.6	-18.9	-13.6	-14.1	-7.3	-49.7	-17.7	-3.4	-54.5
Summer	146.5	-47.6	-75.2	128.0	-43.1	-87.8	121.6	-33.8	-84.2
Autumn	37.5	7.6	-89.1	77.3	121.7	-94.3	73.8	92.1	-92.8

Table 24
Monthly Summary of Projected Percentage Change (%) in Mean, Maximum (Max), and Minimum (Min) Flow (M_{bench}) for the End-of-Century Period (2075–2100). The background color indicates flow magnitude: Red tones signify higher increases or lower decreases, and green tones signify lower increases or higher decreases.

Scenario	Optimistic (SSP1-2.6)			Average (SSP2-4.5)			Pessimistic (SSP5-8.5)		
Month	Mean%	Max%	Min%	Mean%	Max%	Min%	Mean%	Max%	Min%
January	23.3	112.7	-63.4	52.7	126.1	-62.1	64.5	98.1	-61.4
February	17.0	15.8	-36.7	25.2	10.4	-50.1	24.4	18.9	-44.1
March	4.6	-27.2	-16.4	-7.8	-7.3	-24.6	-11.3	-5.6	-52.6
April	-21.6	19.8	36.1	-26.8	2.1	-43.6	-29.8	20.5	-21.5
May	8.8	30.8	15.6	3.0	78.5	-42.9	-2.8	43.4	-13.6
June	184.5	-47.6	-33.1	166.7	-43.1	-70.7	161.3	-33.8	-52.6
July	147.4	311.9	-53.0	127.0	306.6	-82.3	119.1	297.1	-74.2
August	103.0	212.6	-75.2	85.8	209.5	-87.3	79.7	211.5	-84.2
September	84.8	13.8	-75.2	73.4	36.0	-87.5	68.8	12.3	-87.1
October	31.1	-83.1	-86.5	63.3	67.1	-93.7	56.8	78.7	-90.6
November	25.8	7.6	-89.0	83.4	101.2	-92.6	81.3	85.8	-91.5
December	-1.9	52.3	-64.3	65.7	145.7	-88.1	71.6	172.5	-83.4

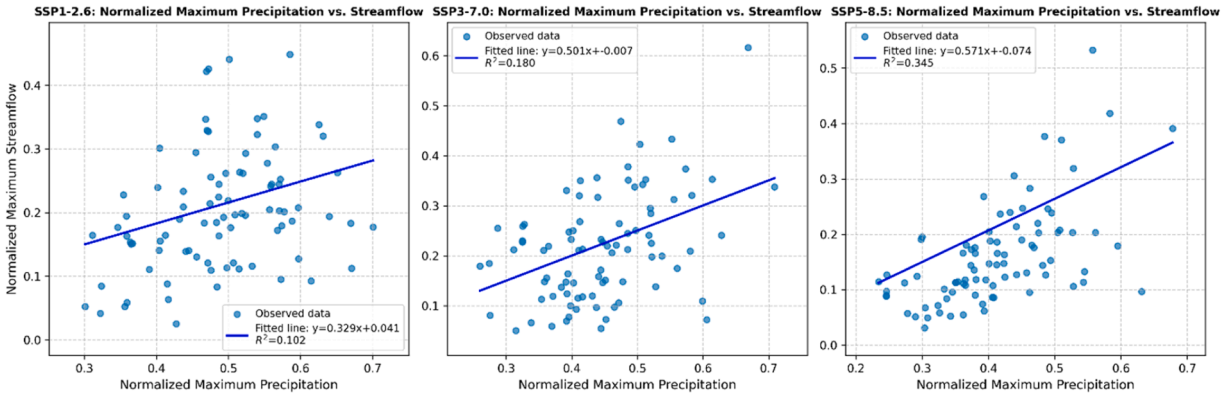

Fig. 17. Normalized maximum precipitation versus normalized maximum streamflow for SSP Scenarios (2025–2100).

4.2. Compounding risks and operational challenges

The acceleration of the hydrological cycle leads to a temporal compression of the hydrograph, shifting flood peaks from April/May to March. This creates an unprecedented dilemma for the basin's extensive dam infrastructure. Operators must drawdown reservoirs earlier for flood safety, reducing the window for full recharge and agricultural supply. While the current modeling framework does not utilize site-specific reservoir rule curves for daily operations, the projected advancement of peak flows suggests a fundamental mismatch with existing management schedules. As supported by the findings of Sha et al. (2024) and Babacan and Yüksek (2024), these physical shifts in inflow timing necessitate a strategic reassessment of reservoir operation schemes. Therefore, our results should be interpreted as a hydroclimatic basis for long-term planning, identifying the need for adaptive management rather than prescribing specific operational changes.

4.3. Exacerbation of water scarcity and drought extremes

The pronounced impact of summer TAS on the hydrological regime (Supplementary Fig. 28) highlights the dominance of evaporative demand over precipitation in determining water stress. Every unit of temperature increase amplifies the reduction in river flow, a feedback mechanism supported by D. Singh et al. (2023) and Yang et al. (2023). This culminates in the catastrophic reduction of minimum monthly discharge projected for 2075–2100 under SSP5–8.5 (Table 16). Such extreme low-flows, also documented by and

Babacan and Yüksek (2024), threaten riverine ecology and increase the risk of saltwater intrusion, necessitating advanced groundwater recharge and irrigation efficiency.

4.4. Process-based drivers of mid-century volatility

The mid-century period (2050–2075) is characterized by the largest net change in average discharge (Fig. 8), representing a phase of maximum hydrological volatility. Beyond a simple reporting of simulation outputs, the underlying physical drivers are identified through a process-based analysis, revealing a fundamental repartitioning of water fluxes. Although precipitation (PR) projections vary among GCMs, the direction of hydrological impact remains consistent due to the clear dominance of thermal forcing over the water balance, a trend further exacerbated by the increasing frequency and severity of regional heatwaves (Rezaee et al., 2025). This 'temperature dominance' is further confirmed by the SHAP sensitivity analysis (Fig. 7), in which parameters governing vertical fluxes—specifically arnoBeta_add (Infiltration), crop_correct (Evapotranspiration), and soildepth_factor (Storage)—demonstrate the highest global importance ($R^2 > 0.90$).

The dominance of these specific parameters aligns with the physical and climatic realities of the semi-arid study area, where land surface temperature dynamics and water availability are strictly governed by soil moisture and vegetation indices (Rezaee et al., 2026). The high sensitivity to these parameters underscores the existence of a physical feedback loop: intensified thermal forcing amplifies potential evapotranspiration (PET), thereby prioritizing vertical moisture losses over lateral runoff. As the hydrological regime transitions from a storage-controlled to an evaporation-dominated system—a shift consistent with findings by Kartal (2024) and Adib and Harun (2022)—future water availability is determined to be primarily governed by PET-driven losses rather than precipitation variability. Consequently, as accurate evapotranspiration estimation remains a fundamental challenge in data-scarce regions (Mohammadnezhad et al., 2025), it is suggested that adaptation strategies prioritize demand-side management as a necessary mitigation response to this thermally-induced depletion of net water resources.

4.5. Reservoir representation and anthropogenic non-stationarity

A critical strength of this study is the integration of custom scenarios for anthropogenic non-stationarity into the modeling framework. The impact of missing operational data for specific upstream reservoirs was systematically quantified by comparing the two calibration benchmarks. The 11.6% systematic bias (Table 6) observed in the M_{bench} (naturalized potential) simulations serves as a proxy for the unquantified buffering effect of these infrastructures. While the KGE= 0.60 for M_{obs} is lower than M_{bench} (KGE=0.71), it represents a successful calibration for this complex environment, consistent with the KGE of 0.57 reported for the Zambezi basin (Burek et al., 2019).

To address the inherent challenge of equifinality—where multiple parameter sets may yield similar outputs—this study utilized a dual-benchmark constraint and SHAP-based verification. By achieving consistent performance across both M_{obs} and M_{bench} using physically-grounded parameters, the risk of mathematical artifacts was minimized. Furthermore, the retention of M_{obs} serves not only to establish a 'realistic uncertainty envelope' but also to explicitly acknowledge the parameter uncertainty boundaries in a human-regulated, data-scarce basin. This prioritization of parameter uncertainty (equifinality) over GCM variance when projecting process-based variables like soil moisture and groundwater is consistent with the findings of Her et al. (2019). As noted by Burek et al. (2019), while explicit regulation data is ideal, our framework remains robust for long-term strategic planning by capturing the overall hydroclimatic trajectory despite these operational constraints.

4.6. Future research directions

Future reliability of these projections can be enhanced by addressing key modeling gaps through targeted technical advancements. A strategic priority involves the integration of Sentinel-1 Synthetic Aperture Radar (SAR) data to independently monitor reservoir dynamics. Given its all-weather imaging capability, Sentinel-1 enables the mapping of water surface area and the derivation of elevation-area-volume relationships, particularly in sub-basins where operational data is unavailable (Tortini et al., 2020). This satellite-based approach provides a concrete pathway to reduce the 11.6% (Table 6) modeling bias identified in this study by enabling the independent calibration of reservoir storage and release patterns. Moreover, future reliability can be enhanced by adopting hybrid data-driven frameworks to manage noise, as demonstrated by (Poursaeid, 2025) using Kalman-filter-driven models, alongside advanced evaluation metrics like the Area Over the Regression ROC (AOC) curve (Tec, 2025) for more rigorous performance validation. Such high-resolution remote sensing integration would transition the current framework from a strategic hydroclimatic outlook toward a more precise operational tool for basin-wide water management.

5. Conclusions

This study quantified the evolving hydrological regime of the Karun-Karkheh-Marzi-e-Gharb basin complex by integrating the Community Water Model (CWatM) with a robust dual-calibration framework. By overcoming significant data constraints and accounting for anthropogenic non-stationarity—including irrigation and reservoir regulation—this research provides a refined scientific basis that extends beyond traditional national meteorological assessments. While existing reports from agencies such as the Iran Meteorological Organization (IRIMO) have primarily focused on macro-scale climatic trends, our findings offer a more granular, physically-based projection of future runoff dynamics, filling a critical information gap for regional water-security planning.

The results reveal a consistent hydrograph transformation driven by thermal forcing across all SSP scenarios. Warmer winters are reducing snow storage and advancing peak flow timing toward late winter, while intensified evapotranspiration outweighs precipitation variability, leading to a net decline in annual water yield and a critical escalation in late-century drought extremes. These projections were achieved through a computationally efficient pipeline (totaling 2250 simulation years on mid-range hardware), demonstrating that rigorous ensemble-based stress-testing is feasible without high-performance computing (HPC) allocations.

Despite its contributions, the study is subject to limitations, notably the coarse 0.5° spatial resolution and the absence of site-specific reservoir rule curves, which influence the precision of results in smaller regulated sub-basins. Furthermore, while the model identifies long-term strategic trends, it is intended as a hydroclimatic outlook rather than a real-time operational decision-support tool.

Ultimately, these findings emphasize that future water security in human-impacted regions will be defined by shifts in timing and extremes. This framework represents a significant step toward informed strategic planning, suggesting that adaptation must prioritize demand-side management and the transition from stationary rules toward adaptive, climate-resilient water allocation.

CRediT authorship contribution statement

Mahdi Mohammadnezhad: Writing – review & editing, Writing – original draft, Visualization, Validation, Software, Methodology, Investigation, Formal analysis, Data curation, Conceptualization. **Mikhail Smilovic:** Writing – review & editing, Supervision, Software, Methodology. **Ali Rezaee:** Writing – review & editing, Validation, Supervision, Conceptualization.

Funding

This research did not receive any specific grant from funding agencies in the public, commercial, or not-for-profit sectors.

Declaration of Generative AI and AI-assisted technologies in the writing process

During the preparation of this work the authors used Gemini in order to review the language (English). After using this tool, the authors reviewed and edited the content as needed and take full responsibility for the content of the publication.

Declaration of Competing Interest

The authors declare that they have no known competing financial interests or personal relationships that could have appeared to influence the work reported in this paper.

Acknowledgments

We are deeply grateful for the institutional support and resources essential to this research. We extend our sincere appreciation to the International Institute of Applied Systems Analysis (IIASA) and ETH Zurich, whose staff and researchers developed the CWatM model central to this study, and provided the collaborative environment and access to modeling facilities that were critical to the successful completion of this work.

Appendix A. Supporting information

Supplementary data associated with this article can be found in the online version at doi:10.1016/j.ejrh.2026.103534.

Data availability

The complete set of pre-processed input data, the final calibrated CWatM model code (including the necessary local modifications for debugging and execution), and the primary simulation results are permanently archived and available at the following GitHub repository: https://github.com/mahdimohammadnezhad/CWatM_modified.

The analysis scripts used for calibration evaluation (SHAP), climate projection processing, multi-scale trend analysis, and figure generation are archived separately to facilitate replication of the study's results: https://github.com/AliRezaee86/River_Discharge_Data.

All raw data used in this study, such as GCM outputs, reanalysis products, and GloFAS data, are available from their respective public domain sources. For further guidance on data preparation and replication of the modeling framework, please contact the corresponding author.

References

Abdi-Dehkordi, M., Bozorg-Haddad, O., Salavitabar, A., Loáiciga, H.A., 2024. Inter-basin water governance by transfer rules based on system dynamics. Theor. Appl. Climatol. 155 (8), 8229–8243. https://doi.org/10.1007/s00704-024-05126-y.

Adib, M.N.M., Harun, S., 2022. Metalearning approach coupled with CMIP6 multi-GCM for future monthly streamflow forecasting. J. Hydrol. Eng. 27 (6), 05022004.

Ahmad, M.-D., Islam, M.A., Masih, I., Muthuwatta, L., Karimi, P., Turral, H., 2009. Mapping basin-level water productivity using remote sensing and secondary data in the Karkheh River Basin, Iran. Water Int. 34 (1), 119–133.

Ayele, G.T., Yu, B., 2025. Comparative analysis of lumped and semi-distributed hydrological models for an upland watershed in Ethiopia. J. Hydrol. Reg. Stud. 60, 102486.

Babacan, H.T., Yüksek, Ö., 2024. Investigation of climate change impacts on daily streamflow extremes in Eastern Black Sea Basin, Turkey. Phys. Chem. Earth Parts A/B/C. 134, 103599.

Beven, K., 2001. How far can we go in distributed hydrological modelling? Hydrol. Earth Syst. Sci. 5 (1), 1–12. https://doi.org/10.5194/hess-5-1-2001.

Boucher, O., Servonnat, J., Albright, A.L., Aumont, O., Balkanski, Y., Bastrikov, V., Bekki, S., Bonnet, R., Bony, S., Bopp, L., Braconnot, P., Brockmann, P., Cadule, P., Caubel, A., Cheruy, F., Codron, F., Cozic, A., Cugnet, D., D'Andrea, F., Vuichard, N., 2020. Presentation and evaluation of the IPSL-CM6A-LR Climate Model. J. Adv. Model. Earth Syst. 12 (7), e2019MS002010. https://doi.org/10.1029/2019MS002010.

Burek, P., Satoh, Y., Kahil, T., Tang, T., Greve, P., Smilovic, M., Guillaumot, L., Wada, Y., 2019. Development of the Community Water Model (CWatM v1. 04) A high-resolution hydrological model for global and regional assessment of integrated water resources management. Geosci. Model Dev. Discuss. 2019, 1–49.

Chang, F.-J., Chang, L.-C., Chen, J.-F., 2023. Artificial Intelligence techniques in hydrology and water resources management. Water 15 (10). https://doi.org/10.3390/w15101846.

Clark, M.P., Slater, A.G., Rupp, D.E., Woods, R.A., Vrugt, J.A., Gupta, H.V., Wagener, T., Hay, L.E., 2008. Framework for Understanding Structural Errors (FUSE): A modular framework to diagnose differences between hydrological models. Water Resour. Res. 44 (12).

Clark, M.P., Nijssen, B., Lundquist, J.D., Kavetski, D., Rupp, D.E., Woods, R.A., Freer, J.E., Gutmann, E.D., Wood, A.W., Brekke, L.D., Arnold, J.R., Gochis, D.J., Rasmussen, R.M., 2015. A unified approach for process-based hydrologic modeling: 1. Modeling concept. Water Resour. Res. 51 (4), 2498–2514. https://doi.org/10.1002/2015WR017198.

Cucchi, M., Weedon, G.P., Amici, A., Bellouin, N., Lange, S., Schmied, H.M., Hersbach, H., Buontempo, C., 2020. WFDE5: bias adjusted ERA5 reanalysis data for impact studies. Earth Syst. Sci. Data Discuss. 2020, 1–32.

Deb, K., Pratap, A., Agarwal, S., Meyarivan, T., 2002. A fast and elitist multiobjective genetic algorithm: NSGA-II. IEEE Trans. Evolut. Comput. 6 (2), 182–197.

Dione, P.M., Faye, C., Mohamed, A., Alarifi, S.S., Mohammed, M.A.A., 2024. Assessment of the impact of climate change on current and future flows of the ungauged Aga-Foua-Djilas watershed: a comparative study of hydrological models CWatM under ISIMIP and HMF-WA. Appl. Water Sci. 14 (7), 163. https://doi.org/10.1007/s13201-024-02219-x.

Döll, P., Lehner, B., 2002. Validation of a new global 30-min drainage direction map. J. Hydrol. 258 (1–4), 214–231.

Döll, P., Siebert, S., 2002. Global modeling of irrigation water requirements. Water Resour. Res. 38 (4), 1–8.

Du, C., Sun, F., Yu, J., Liu, X., Chen, Y., 2016. New interpretation of the role of water balance in an extended Budyko hypothesis in arid regions. Hydrol. Earth Syst. Sci. 20 (1), 393–409. https://doi.org/10.5194/hess-20-393-2016.

Dunne, J.P., Horowitz, L.W., Adcroft, A.J., Ginoux, P., Held, I.M., John, J.G., Krasting, J.P., Malyshev, S., Naik, V., Paulot, F., Shevliakova, E., Stock, C.A., Zadeh, N., Balaji, V., Blanton, C., Dunne, K.A., Dupuis, C., Durachta, J., Dussin, R., Zhao, M., 2020. The GFDL Earth System Model Version 4.1 (GFDL-ESM 4.1): Overall Coupled Model Description and Simulation Characteristics. J. Adv. Model. Earth Syst. 12 (11), e2019MS002015. https://doi.org/10.1029/2019MS002015.

Elvidge, C.D., Tuttle, B.T., Sutton, P.S., Baugh, K.E., Howard, A.T., Milesi, C., Bhaduri, B.L., Nemani, R., 2007. Global distribution and density of constructed impervious surfaces. Sensors 7 (9), 1962–1979.

Fao, I., ISRIC, I., 2012. Jrc: Harmonized world soil database (version 1.2). FAO, *Rome, Italy and IIASA, Laxenburg, Austria*.

Fortin, F.-A., De Rainville, F.-M., Gardner, M.-A. G., Parizeau, M., Gagné, C., 2012. DEAP: Evolutionary algorithms made easy. J. Mach. Learn. Res. 13 (1), 2171–2175.

Gao, J., 2017. Downscaling global spatial population projections from 1/8-degree to 1-km grid cells. Natl. Cent. Atmos. Res. 1105 (Boulder, CO, USA).

Geological Survey Center for Earth Resources Observation and Science (USGS). (2002). *Hydro1k*.

Ghobadi, Y., Pradhan, B., Sayyad, G.A., Kabiri, K., Falamarzi, Y., 2015. Simulation of hydrological processes and effects of engineering projects on the Karkheh River Basin and its wetland using SWAT, 2009 Quat. Int. 374, 144–153.

Gidden, M.J., Fujimori, S., van den Berg, M., Klein, D., Smith, S.J., van Vuuren, D.P., Riahi, K., 2018. A methodology and implementation of automated emissions harmonization for use in Integrated Assessment Models. Environ. Model. & Softw. 105, 187–200.

Gleeson, T., Smith, L., Moosdorf, N., Hartmann, J., Dürr, H.H., Manning, A.H., van Beek, L.P.H., Jellinek, A.M., 2011. Mapping permeability over the surface of the Earth. Geophys. Res. Lett. 38 (2).

Gleeson, T., Moosdorf, N., Hartmann, J., van Beek, L.P.H. van, 2014. A glimpse beneath earth's surface: GLobal HYdrogeology MaPS (GLHYMPS) of permeability and porosity. Geophys. Res. Lett. 41 (11), 3891–3898.

Gleick, P.H., Cooley, H., 2009. The world's water 2008-2009: The biennial report on freshwater resources, 6. Island Press.

Granata, F., 2019. Evapotranspiration evaluation models based on machine learning algorithms—A comparative study. Agric. Water Manag. 217, 303–315. https://doi.org/10.1016/j.agwat.2019.03.015.

GRDC. (2007). Major River Basins of the World/Global Runoff Data Centre. GRDC. 2nd, *Rev. Ext. Ed. Koblenz, Germany: Federal Institute of Hydrology (BfG)*.

Grimaldi, S., Salamon, P., Disperati, J., Zsoter, E., Russo, C., Ramos, A., Carton De Wiart, C., Barnard, C., Hansford, E., Gomes, G., 2022. River discharge and related historical data from the Global Flood Awareness System. v4. 0. Eur. Comm. Jt. Res. Cent. (JRC). ⟨Https://Cds.Climate.Copernicus.Eu/Cdsapp⟩ (URL).

Gupta, H.V., Kling, H., Yilmaz, K.K., Martinez, G.F., 2009. Decomposition of the mean squared error and NSE performance criteria: Implications for improving hydrological modelling. J. Hydrol. 377 (1–2), 80–91.

Hansen, M.C., Potapov, P.V., Moore, R., Hancher, M., Turubanova, S.A., Tyukavina, A., Thau, D., Stehman, S.V., Goetz, S.J., Loveland, T.R., 2013. High-resolution global maps of 21st-century forest cover change. Science 342 (6160), 850–853.

Her, Y., Yoo, S.-H., Cho, J., Hwang, S., Jeong, J., Seong, C., 2019. Uncertainty in hydrological analysis of climate change: multi-parameter vs. multi-GCM ensemble predictions. Sci. Rep. 9 (1), 4974.

Hirpa, F.A., Salamon, P., Beck, H.E., Lorini, V., Alfieri, L., Zsoter, E., Dadson, S.J., 2018. Calibration of the Global Flood Awareness System (GloFAS) using daily streamflow data. J. Hydrol. 566, 595–606.

Hrachowitz, M., Savenije, H.H.G., Blöschl, G., McDonnell, J.J., Sivapalan, M., Pomeroy, J.W., Arheimer, B., Blume, T., Clark, M.P., Ehret, U., 2013. A decade of Predictions in Ungauged Basins (PUB)—a review. Hydrol. Sci. J. 58 (6), 1198–1255.

Huntington, T.G., 2006. Evidence for intensification of the global water cycle: Review and synthesis. J. Hydrol. 319 (1), 83–95. https://doi.org/10.1016/j.jhydrol.2005.07.003.

Huscroft, J., Gleeson, T., Hartmann, J., Börker, J., 2018. Compiling and mapping global permeability of the unconsolidated and consolidated Earth: GLobal HYdrogeology MaPS 2.0 (GLHYMPS 2.0). Geophys. Res. Lett. 45 (4), 1897–1904.

Iqbal, Z., Shahid, S., Ismail, T., Sa'adi, Z., Farooque, A., Yaseen, Z.M., 2022. Distributed hydrological model based on machine learning algorithm: Assessment of climate change impact on floods. Sustainability 14 (11), 6620.

Jarvis, A., Reuter, H.I., Nelson, A., & Guevara, E. (2008). Hole-filled SRTM for the globe Version 4. *Available from the CGIAR-CSI SRTM 90m Database* (⟨Http://Srtm⟩. Csi. Cgiar. Org), 15(25–54), 5.

Jones, B., O'Neill, B.C., 2016. Spatially explicit global population scenarios consistent with the Shared Socioeconomic Pathways. Environ. Res. Lett. 11 (8), 084003.

Kartal, V., 2024. Machine learning-based streamflow forecasting using CMIP6 scenarios: Assessing performance and improving hydrological projections and climate change. Hydrol. Process. 38 (6), e15204.

Khan, M., Khan, A.U., Khan, S., Khan, F.A., 2023. Assessing the impacts of climate change on streamflow dynamics: A machine learning perspective. Water Sci. Technol. 88 (9), 2309–2331. https://doi.org/10.2166/wst.2023.340.
Kim, H., Yoshimura, K., Chang, E., Famiglietti, J.S., Oki, T., 2012. Century long observation constrained global dynamic downscaling and hydrologic implication. AGU Fall Meet. Abstr. 2012. GC31D-02.
Klein Goldewijk, K., Beusen, A., Doelman, J., Stehfest, E., 2017. Anthropogenic land use estimates for the Holocene–HYDE 3.2. Earth Syst. Sci. Data 9 (2), 927–953.
Kling, H., Fuchs, M., Paulin, M., 2012. Runoff conditions in the upper Danube basin under an ensemble of climate change scenarios. J. Hydrol. 424, 264–277.
Kraft, P., Vaché, K.B., Frede, H.-G., Breuer, L., 2011. CMF: A Hydrological Programming Language Extension For Integrated Catchment Models. Environ. Model. & Softw. 26 (6), 828–830. https://doi.org/10.1016/j.envsoft.2010.12.009.
Kummu, M., Taka, M., Guillaume, J.H.A., 2018. Gridded global datasets for gross domestic product and human development index over 1990–2015. Sci. Data 5 (1), 1–15.
Lange, S., 2019. Trend-preserving bias adjustment and statistical downscaling with ISIMIP3BASD (v1. 0). Geosci. Model Dev. 12 (7), 3055–3070.
Lange, S., 2021. ISIMIP3BASD. Zenodo. https://doi.org/10.5281/zenodo.4686991.
Lehner, B., Liermann, C.R., Revenga, C., Vörösmarty, C., Fekete, B., Crouzet, P., Döll, P., Endejan, M., Frenken, K., Magome, J., 2011. High-resolution mapping of the world's reservoirs and dams for sustainable river-flow management. Front. Ecol. Environ. 9 (9), 494–502.
Madhushani, C., Dananjaya, K., Ekanayake, I.U., Meddage, D.P.P., Kantamaneni, K., Rathnayake, U., 2024. Modeling streamflow in non-gauged watersheds with sparse data considering physiographic, dynamic climate, and anthropogenic factors using explainable soft computing techniques. J. Hydrol. 631, 130846. https://doi.org/10.1016/j.jhydrol.2024.130846.
Marjanizadeh, S., Qureshi, A.S., Turral, H., Talebzadeh, P., 2010. From Mesopotamia to the third millennium: The historical trajectory of water development and use in the Karkheh River Basin. In: Iran, 135. IWMI.
Masih, I., Maskey, S., Uhlenbrook, S., Smakhtin, V., 2011. Impact of upstream changes in rain-fed agriculture on downstream flow in a semi-arid basin. Agric. Water Manag. 100 (1), 36–45.
Matiu, M., Crespi, A., Bertoldi, G., Carmagnola, C.M., Marty, C., Morin, S., Schöner, W., Cat Berro, D., Chiogna, G., De Gregorio, L., Kotlarski, S., Majone, B., Resch, G., Terzago, S., Valt, M., Beozzo, W., Cianfarra, P., Gouttevin, I., Marcolini, G., Weilguni, V., 2021. Observed snow depth trends in the European Alps: 1971–2019. Cryosphere 15 (3), 1343–1382. https://doi.org/10.5194/tc-15-1343-2021.
Mauritsen, T., Bader, J., Becker, T., Behrens, J., Bittner, M., Brokopf, R., Brovkin, V., Claussen, M., Crueger, T., Esch, M., Fast, I., Fiedler, S., Fläschner, D., Gayler, V., Giorgetta, M., Goll, D.S., Haak, H., Hagemann, S., Hedemann, C., Roeckner, E., 2019. Developments in the MPI-M Earth System Model version 1.2 (MPI-ESM1.2) and Its Response to Increasing CO(2). J. Adv. Model. Earth Syst. 11 (4), 998–1038. https://doi.org/10.1029/2018MS001400.
Messager, M.L., Lehner, B., Grill, G., Nedeva, I., Schmitt, O., 2016. Estimating the volume and age of water stored in global lakes using a geo-statistical approach. Nat. Commun. 7 (1), 13603.
Mohammadnezhad, M., Davary, K., Shirazi, P., Rezvanpour, M.J., Hasheminia, S.M., 2025. A novel hybrid model for actual evapotranspiration estimation in data-scarce arid regions: Integrating modified Budyko and machine learning models using deep learning. Sci. Total Environ. 1001, 180438. https://doi.org/10.1016/j.scitotenv.2025.180438.
Muller, J.-P., López, G., Watson, G., Shane, N., Kennedy, T., Yuen, P., Lewis, P., Fischer, J., Guanter, L., Domench, C., 2012. The ESA GlobAlbedo Project for mapping the Earth's land surface albedo for 15 years from European sensors. Geophys. Res. Abstr. 13, 10969.
Portmann, F.T., Siebert, S., Döll, P., 2010. MIRCA2000—Global monthly irrigated and rainfed crop areas around the year 2000: A new high-resolution data set for agricultural and hydrological modeling. Glob. Biogeochem. Cycles 24 (1).
Poursaeid, M., 2025. Unraveling the water quality-ecosystem nexus using Kalman filter-driven models and feature analysis under uncertainty. J. Hydrol. 657, 133092. https://doi.org/10.1016/j.jhydrol.2025.133092.
Rezaee, A., Goodarzi, M.R., Etemadfard, H., Alavizadeh, M., 2025. A copula-based framework for assessing heat wave extremes and probability of occurrence in Iran: implications for climate change. Stoch. Environ. Res. Risk Assess. 39 (6), 2461–2477. https://doi.org/10.1007/s00477-025-02979-1.
Rezaee, A., Goodarzi, M.R., Alavizadeh, S.M., Goldani, M., 2026. Machine learning insights into land surface temperature variability and prediction: a spatiotemporal approach with feature importance and uncertainty analysis. Environ. Monit. Assess. 198 (5), 480. https://doi.org/10.1007/s10661-026-15205-4.
Riahi, K., Van Vuuren, D.P., Kriegler, E., Edmonds, J., O'neill, B.C., Fujimori, S., Bauer, N., Calvin, K., Dellink, R., Fricko, O., 2017. The Shared Socioeconomic Pathways and their energy, land use, and greenhouse gas emissions implications: An overview. Glob. Environ. Change 42, 153–168.
Samaniego, L., Kumar, R., Thober, S., Rakovec, O., Zink, M., Wanders, N., Eisner, S., Müller Schmied, H., Sutanudjaja, E.H., Warrach-Sagi, K., 2017. Toward seamless hydrologic predictions across spatial scales. Hydrol. Earth Syst. Sci. 21 (9), 4323–4346.
Sellar, A.A., Jones, C.G., Mulcahy, J.P., Tang, Y., Yool, A., Wiltshire, A., O'Connor, F.M., Stringer, M., Hill, R., Palmieri, J., Woodward, S., de Mora, L., Kuhlbrodt, T., Rumbold, S.T., Kelley, D.I., Ellis, R., Johnson, C.E., Walton, J., Abraham, N.L., Zerroukat, M., 2019. UKESM1: Description and Evaluation of the U.K. Earth System Model. J. Adv. Model. Earth Syst. 11 (12), 4513–4558. https://doi.org/10.1029/2019MS001739.
Sha, J., Chang, Y., Liu, Y., 2024. Hydrological Response to Climate Change: McGAN for Multi-Site Scenario Weather Series Generation and LSTM for Streamflow Modeling. Atmosphere 15 (11).
Siebert, S., Döll, P., Hoogeveen, J., Faures, J.-M., Frenken, K., Feick, S., 2005. Development and validation of the global map of irrigation areas. Hydrol. Earth Syst. Sci. 9 (5), 535–547.
Siebert, S., Burke, J., Faures, J.-M., Frenken, K., Hoogeveen, J., Döll, P., Portmann, F.T., 2010. Groundwater use for irrigation–a global inventory. Hydrol. Earth Syst. Sci. 14 (10), 1863–1880.
Šiklomanov, I.A., 1997. Comprehensive Assessment of the Freshwater Resources of the World. WMO.
Singh, D., Vardhan, M., Sahu, R., Chatterjee, D., Chauhan, P., Liu, S., 2023. Machine-learning-and deep-learning-based streamflow prediction in a hilly catchment for future scenarios using CMIP6 GCM data. Hydrol. Earth Syst. Sci. 27 (5), 1047–1075.
Steinfeld, H., Gerber, P., Wassenaar, T.D., Castel, V., De Haan, C., 2006. Livestock's long shadow: environmental issues and options. Food & Agriculture Org.
Tec, M., 2025. ROC analysis for classification and prediction in practice. J. Am. Stat. Assoc. 120 (549), 585–586. https://doi.org/10.1080/01621459.2024.2423434.
Tortini, R., Noujdina, N., Yeo, S., Ricko, M., Birkett, C.M., Khandelwal, A., Kumar, V., Marlier, M.E., Lettenmaier, D.P., 2020. Satellite-based remote sensing data set of global surface water storage change from 1992 to 2018. Earth Syst. Sci. Data 12 (2), 1141–1151. https://doi.org/10.5194/essd-12-1141-2020.
Tursun, A., Xie, X., Wang, Y., Peng, D., Liu, Y., Zheng, B., Wu, X., Nie, C., 2024. Streamflow prediction in human-regulated catchments using multiscale deep learning modeling with anthropogenic similarities. Water Resour. Res. 60 (9) e2023WR036853.
Wang, J., Zhou, L., Ma, C., Sun, W., 2025. Analyzing the effects of climate change and human activities on streamflow in a North China arid basin: a machine learning perspective considering model structural uncertainty. Theor. Appl. Climatol. 156 (2), 123. https://doi.org/10.1007/s00704-025-05352-y.
Wint, G.R.W., & Robinson, T.P. (2007). *Gridded livestock of the world. Food and Agriculture Organization of the United Nations, Rome.*
Wu, H., Kimball, J.S., Mantua, N., Stanford, J., 2011. Automated upscaling of river networks for macroscale hydrological modeling. Water Resour. Res. 47 (3).
Yang, H., Zhang, Z., Liu, X., Jing, P., 2023. Monthly-scale hydro-climatic forecasting and climate change impact evaluation based on a novel DCNN-Transformer network. Environ. Res. 236, 116821.
Yao, S., Chen, C., Chen, Q., Zhang, J., He, M., 2023. Combining process-based model and machine learning to predict hydrological regimes in floodplain wetlands under climate change. J. Hydrol. 626, 130193.
Yukimoto, S., Kawai, H., Koshiro, T., Oshima, N., Yoshida, K., Urakawa, S., Tsujino, H., Deushi, M., Tanaka, T., Hosaka, M., 2019. The Meteorological Research Institute Earth System Model version 2.0, MRI-ESM2. 0: Description and basic evaluation of the physical component. J. Meteorol. Soc. Jpn. Ser. II 97 (5), 931–965.
Zareian, M.J., & Salem, F. (2022). *Simulation of climate change effects on streamflow based on a deep learning network (case study: a semi-arid region in central Iran).*
Zhang, Y., Schaap, M.G., 2017. Weighted recalibration of the Rosetta pedotransfer model with improved estimates of hydraulic parameter distributions and summary statistics (Rosetta3). J. Hydrol. 547, 39–53.

Zhu, F., Hou, T., Zhu, O., Sun, Y., Liu, W., Zhao, L., Guo, X., Li, M., Zhong, P., 2025. Multi-step ahead probabilistic runoff forecasting with SHAP interpretability: a GPR-enhanced deep learning ensemble approach integrating teleconnection factors. Environ. Model. & Softw. 193, 106647. https://doi.org/10.1016/j.envsoft.2025.106647.

Zhu, F., Zhu, O., Han, M., Liu, W., Guo, X., Hou, T., Zhao, L., Xu, C., Zhong, P., 2025. A hybrid process-data driven framework for real-time hydrological forecasting with interpretable deep learning. J. Hydrol. 662, 134082. https://doi.org/10.1016/j.jhydrol.2025.134082.

Zounemat-Kermani, M., Kheimi, M., 2026. Explainable Artificial Intelligence in Hydrology: A Review. Water Resour. Manag. 40 (3), 106. https://doi.org/10.1007/s11269-025-04435-9.